

学位論文

Development of a Vibrationally-Electronically Doubly
Resonant Sum-Frequency Generation Spectrometer and
its Application to Aromatic Thin Films

振動電子二重共鳴 SFG 分光装置の開発と芳香族薄
膜への応用

2011 年

広島大学大学院理学研究科

化学専攻

前田 俊樹

目次

1. 主論文

Development of Vibrationally-Electronically Doubly Resonant Sum-Frequency Generation Spectrometer and its Application to Aromatic Thin Films

(振動電子二重共鳴 SFG 分光装置の開発と芳香族薄膜への応用)

前田俊樹

2. 公表論文

(1) IR-UV Sum-Frequency Generation Spectrometer with a wide tunability of the UV probe

Toshiki Maeda and Taka-aki Ishibashi

Applied Spectroscopy, **61**, 459-464 (2007).

(2) Identification of chemical species of fluorescein isothiocyanate isomer-I (FITC) monolayers on platinum by doubly resonant sum-frequency generation spectroscopy

Toshiki Maeda, Tetsuhiko Nagahara, Misako Aida and Taka-aki Ishibashi

Journal of Raman Spectroscopy, **39**, 1694-1702 (2008).

主論文

Development of Vibrationally-Electronically Doubly Resonant Sum-Frequency
Generation Spectrometer and its Application to Aromatic Thin Films

Toshiki Maeda

Center for Quantum Life Sciences,

and

Department of Chemistry, Graduate School of Science, Hiroshima University

Acknowledgements

I would like to express my great gratitude to my supervisor, Professor Taka-aki Ishibashi for his valuable discussions, indispensable guidance and continuous encouragement over these seven years. Without his persistent help, this dissertation would not have been possible. He also gave me a chance to meet many scientists through various academic meetings.

I am deeply grateful to Professor Misako Aida who have provided helpful information and opinions to sort out my thought and supported me throughout this work.

I would like to thank Dr. Tetsuhiko Nagahara for his invaluable advices and giving me a lot of experimental techniques of SFG experiments.

I wish to thank Professor Yukio Furukawa, Department of Chemistry, School of Science and Engineering, Waseda University. He gave me a chance to study thin films of PTCDI derivatives deposited on SiO₂ and Si/SiO₂ substrates.

I warmly thank to Dr. Yoshinobu Hosoi and Mr. Nozomu Hashimoto for sending me organic thin films on various substrates and measuring ATR-IR spectra and for their helpful information.

I am much obliged to Dr. Masato Tanaka, Dr. Toshiko Miyake and Dr. Tomoki Yoshida for their useful questions and discussions.

I would like to express my appreciation to Mr. Masayuki Ohisa and Mr. Kazuaki Sakamune for their help in many aspects, especially in software and computer applications.

I would like to thank Dr. Tomonori Yamada for variable discussions and spending common times for these six and a half years as my roommates.

I would also like to thank all the members of our research group for valuable discussions and their kindness.

I gratefully appreciate the financial support of CREST (Core Research for Evolutional Science and Technology) that made possible the completion of my thesis.

Finally, I wish to thank my parents, grandfather, grandmother, sister and brother for encouraging me and allowing me to continue studying.

Contents

| | |
|---|----|
| Chapter 1. General Introduction | 1 |
| 1.1 Introduction..... | 2 |
| 1.2 Vibrational sum-frequency generation spectroscopy..... | 7 |
| References..... | 13 |
| | |
| Chapter 2. Development of an Infrared-Ultraviolet/Visible Sum-Frequency Generation Spectrometer with a Wide Tunability of the Ultraviolet and Visible Probes | 17 |
| 2.1 Introduction..... | 18 |
| 2.2 Infrared-Ultraviolet sum-frequency generation spectrometer..... | 19 |
| 2.3 Infrared-Ultraviolet sum-frequency generation spectra of a <i>p</i> -mercaptobenzoic acid monolayer on gold..... | 24 |
| 2.4 Conclusion..... | 28 |
| References..... | 29 |
| | |
| Chapter 3. Chemical Species of Fluorescein Isothiocyanate Isomer-I (FITC) Monolayers on Platinum Probed by Doubly Resonant Sum-Frequency Generation Spectroscopy | 37 |
| 3.1 Introduction..... | 38 |
| 3.2 Experimental..... | 39 |
| 3.3 Vibrational SFG spectra and DR-SFG excitation profiles of FITC monolayers on platinum..... | 40 |
| 3.4 Vibrational assignments of the vibrational SFG bands..... | 44 |
| 3.5 Fluorescence excitation spectra of FITC monolayers on platinum..... | 46 |
| 3.6 Summary..... | 48 |

| | |
|--|-----------|
| Appendix A. Fresnel factors..... | 49 |
| Appendix B. Improvement in measuring of vibrational SFG spectra and DR-SFG excitation profiles of the FITC monolayer on platinum..... | 51 |
| References..... | 66 |
| | |
| Chapter 4. Doubly Resonant Sum-Frequency Generation Spectroscopy on Thin Films of N, N'-bis(octyl)perylene-3,4,9,10-tetracarboxylic diimide on SiO₂ Substrates | 69 |
| 4.1 Introduction..... | 70 |
| 4.2 Experimental..... | 72 |
| 4.3 Theory..... | 73 |
| 4.4 Results and Discussion..... | 76 |
| 4.5 Conclusion..... | 80 |
| Appendix. Fresnel coefficients for organic thin films on substrates..... | 81 |
| References..... | 94 |
| | |
| Chapter 5. General Conclusion | 97 |

Chapter 1. General Introduction

1.1 Introduction

An interface can be found everywhere. Chemical and physical properties at interfaces are among the central themes in modern chemical research. All the properties and processes at interfaces are usually different from those in the bulk phase. For example, the atomic array of the single-crystal surface differs from that of the bulk. To measure the interface properties, the method with high surface sensitivity and surface selectivity is needed because the absolute number of surface species is quite small (less than 10^{15} per cm^2).

Interface properties have been widely studied by various methods such as electron energy loss spectroscopy (EELS), infrared reflection absorption spectroscopy (IRAS) surface enhanced Raman spectroscopy (SERS), X-ray photoelectron spectroscopy (XPS) and so on. Though these methods have brought great advances to our understanding of the interface properties, they have restrictions for measurement conditions. High vacuum environment, for example, is needed for EELS and XPS. For IRAS, ellipsometry, or methods which rely on evanescent fields, their surface sensitivity is at best on the order of the wavelength of the light, i.e., several hundreds of nanometers or even micrometers. SERS requires rough surfaces and is limited to a small number of substrate materials [1]. On the other hand, even-ordered nonlinear spectroscopy is a powerful technique to probe the properties of interfaces. This technique overcomes all the disadvantages mentioned above.

What has attracted much attention in the second-order nonlinear process are second harmonic generation (SHG) and sum-frequency generation (SFG). These techniques have high surface specificity and wide applicability. SFG (SHG) as a surface analytical tool has a number of clear advantages [2,3]. It can be used to probe all types of interfaces as long as they can be accessible to lights. The high surface specificity together with the submonolayer sensitivity permits spectroscopic study of an interface even if the associated bulk absorbs lights in the same spectral region. The SFG output is highly

directional, so that spatial filtering can be employed in addition to spectral filtering to suppress the unwanted luminescence and scattering background noise. The vacuum environment is not required for the measurement.

In vibrational SFG experiments, visible and IR lights are used as probe ones and are used to generate an SFG signal of the sum-frequency of the two probes. Vibrational SFG spectroscopy is based on a vibrational resonance between the photon energy of an infrared probe and the vibrational energy of molecules at interfaces (Figure 1.1 (a)). Under the electric-dipole approximation, the SFG (SHG) process is forbidden in a medium with inversion symmetry but is allowed at an interface where inversion symmetry is broken, so that the process is surface specific. When we choose visible probe frequency so that SFG frequency is in resonance with electronic absorption of interface species, vibrational SFG band intensities can be further enhanced (Figure 1.1 (b)). Such further enhanced SFG is called vibrationally-electronically doubly-resonant SFG, in short DR-SFG. The DR-SFG process may be regarded as coherent and consecutive processes of infrared absorption and resonance Raman. There are several features of DR-SFG. Signal enhancement due to electronically-resonant effect improves the sensitivity of SFG. The enhancement is expected only for species that have electronic absorption at the SFG frequency. So DR-SFG offers a kind of molecular selectivity to SFG. An electronic spectrum of interface species for each vibrational band can be obtained by measuring visible probe frequency dependence of vibrational SFG band amplitude. The DR-SFG excitation spectra thus obtained give us information on the electronic structure of species. The fourth feature is that DR-SFG allows us to detect chirality of thin films. However, in this case, SFG loses interface specificity. In my doctoral work, I have focused the development (a) and applications (b,c) of DR-SFG spectroscopy.

(a) Construction of an SFG spectrometer designed for DR-SFG

Targets of DR-SFG are limited by what wavelength of visible probe is available.

Most of vibrational SFG spectrometers in existence are lacking in wavelength tunability in the visible probe although there are a very few exceptions [4,5]. The visible probe wavelengths of them are 800 nm or 532 nm depending on whether their probe laser is Ti:sapphire- or Nd:YAG- based system. Therefore, so far, applications of DR-SFG have been limited to dye molecules that have electronic absorption at around 530 nm [6,7]. In order to apply DR-SFG to a variety of molecular interfaces, I started my work by constructing my own vibrational SFG spectrometers that has a wide and continuous tunability of the visible probe. The wavelengths of the ultraviolet (UV) and visible probes are tunable in the range of 235-390, 400, 420-795 nm. As the result of the ultraviolet extension, most aromatic interface species, including biologically important nucleobases and aromatic amino acids, become targets of DR-SFG. In spite of the potential ability of the use of the UV probe, few experimental reports regarding IR-UV SFG spectroscopy has been published [8,9]. Therefore, it is worth conducting DR-SFG spectroscopy in the UV region to demonstrate the features of DR-SFG in the UV region. The developed spectrometer has an important feature other than its wavelength tunability: the multiplex SFG method. In this method, the broad-bandwidth infrared probe and narrow-bandwidth visible probe are used to generate the broad-bandwidth SFG signal. The generated signal is analyzed with a spectrograph equipped with a multichannel detector. This scheme allows us a short data-acquisition time, thus improves the sensitivity of the spectrometer. In our case, about 200 wavenumber wide spectrum can be obtained by one measurement. Test measurements were conducted on a *p*-mercaptobenzoic acid monolayer on a gold substrate to examine the effect of IR-UV DR-SFG.

(b) Identification of surface chemical species by means of DR-SFG electronic excitation profile

DR-SFG spectroscopy has several advantages including the utilization of DR-SFG electronic excitation profile to identify chemical species co-existing on the same substrate. A DR-SFG electronic excitation profile for a certain vibrational band can be obtained by plotting of the vibrationally-resonant SFG amplitude as a function of the SFG wavelength. The electronic excitation profile offers information on the electronic structure of the chemical species that the vibrational band belongs to. I measured DR-SFG electronic excitation profiles for monolayers of fluorescein isothiocyanate isomer-I (FITC) on platinum substrates (Figure 1.2). Fluorescein dye is known to take a variety of protolytic forms in aqueous solutions. Measuring IR-VIS DR-SFG excitation profile for the vibrational bands of the sample, we found that there were two chemical species of FITC whose protolytic types were different each other. This research demonstrates the molecular selectivity of DR-SFG such that a vibrational band of a target molecule can be dominantly emphasized if the wavelength of a visible probe is chosen for DR-SFG for the particular molecule and DR-SFG electronic excitation profiles offer useful information on the electronic structures of interface species.

(c) DR-SFG spectroscopy of organic semiconductor thin films on silica substrates

In this study, I applied DR-SFG spectroscopy to thin-layer samples of organic semiconductor deposited on silica substrates. The samples are N,N'-bis(octyl)perylene-3,4,9,10-tetracarboxylic diimide (PTCDI-C₈, Figure 1.3) thin layers on silica substrates. PTCDI-C₈ is an organic semiconductor material used in organic field effect transistors (OFETs). The bulk layer of PTCDI-C₈ is known to form the center of inversion and hence is SFG inactive. If an SFG signal is obtained from a thin film of PTCDI-C₈, the primary source of the signal should be two interfaces, i.e. the air-semiconductor and semiconductor-silica interfaces. To estimate the extent to which each interface contributes

to the signal, we have examined the thickness dependence of the SFG signal. The quantitative analysis of the thickness dependence has been performed using a model for the effective SFG susceptibility of a thin film that is formulated based on the Fresnel coefficients [10,11]. The analysis was also extended to an advanced model that includes a contribution from the electric quadrupole of the bulk layer. The quadrupole contribution is beyond the electric-dipole approximation.

In the next section, the elementary description of a vibrational SFG process will be given for the convenience of later discussion.

1.2 Vibrational sum-frequency generation spectroscopy

SFG spectroscopy is a means to obtain the information at an interface [1-3,6,12-15]. Vibrational SFG is now widely used to investigate molecular structures of interface species because it permits interface-specific observation of vibrational spectra. In a typical vibrational SFG experiment, two probe lights, one at frequency ω_{VIS} in the visible or UV region and the other at frequency ω_{IR} in the IR region, overlapped spatially and temporally on a target interface, and then an SFG signal with the sum-frequency of the two incident probe frequencies ($\omega_{\text{SFG}} = \omega_{\text{VIS}} + \omega_{\text{IR}}$) is generated. The schematic diagram for the generation of an SFG signal is shown in Figure 1.4. Because SFG is a second order process, under the electric-dipole approximation, it is forbidden in bulk media with inversion symmetry but is allowed at interfaces where the inversion symmetry is broken. Therefore, the SFG signal from an interface can be selectively obtained under the electric-dipole approximation. SFG signal intensity increases when the IR probe is in resonance with a vibrational mode of a molecule at an interface (Figure 1.1 (a)). Hence, a vibrational spectrum of interfacial species can be obtained by measuring the signal intensity as a function of the IR probe frequency.

The SFG signal is generated in a certain direction on the basis of the conservation of momentum parallel to the surface:

$$k_{\text{SF}}^{\parallel} = k_{\text{VIS}}^{\parallel} + k_{\text{IR}}^{\parallel} \quad (1-1)$$

or

$$k_{\text{SF}} \sin \theta_{\text{SF}} = k_{\text{VIS}} \sin \theta_{\text{VIS}} + k_{\text{IR}} \sin \theta_{\text{IR}} \quad (1-2)$$

where k^{\parallel} is the component of the wavevector ($2\pi/\lambda$) parallel to the surface. The notation θ_{VIS} and θ_{IR} are the incidence angles measured from the surface normal of the input visible and IR laser beams, respectively. θ_{SF} is the emission angle of an SFG signal. Thus, the direction of propagation is necessarily determined by the incidence angles and the frequencies of input lasers.

The dipole moment of a molecule is a function of the external electric field (\mathbf{E}) and it can be expressed by a series expansion:

$$\boldsymbol{\mu} = \boldsymbol{\mu}_0 + \alpha \cdot \mathbf{E} + \beta : \mathbf{E}\mathbf{E} + \gamma : \mathbf{E}\mathbf{E}\mathbf{E} + \dots \quad (1-3)$$

where $\boldsymbol{\mu}_0$, α , β and γ is the static dipole moment, molecular linear polarizability, first and second molecular hyperpolarizabilities, respectively. The term $\alpha \cdot \mathbf{E}$ stands for the linear response to the incident electromagnetic field, while other terms in eq. (1-3) characterize the nonlinear response. The abbreviations of $\alpha \cdot \mathbf{E}$ and $\beta : \mathbf{E}\mathbf{E}$ denote $\sum_{ij} \alpha_{ij} E_j$ and $\sum_{ijk} \beta_{ijk} E_j E_k$, respectively. The third or more terms are similarly contracted.

The total polarization can be expressed in terms of the dipole moment per unit volume as follows:

$$\begin{aligned} \mathbf{P} &= \mathbf{P}^{(0)} + \mathbf{P}^{(1)} + \mathbf{P}^{(2)} + \mathbf{P}^{(3)} + \dots \\ &= \mathbf{P}^{(0)} + \varepsilon_0 (\chi^{(1)} \cdot \mathbf{E} + \chi^{(2)} : \mathbf{E}\mathbf{E} + \chi^{(3)} : \mathbf{E}\mathbf{E}\mathbf{E} + \dots) \end{aligned} \quad (1-4)$$

where $\mathbf{P}^{(0)}$ is the static polarization and $\chi^{(i)}$ is the i th-order susceptibility. It is the third term that is responsible for SFG. The second-order nonlinear susceptibility $\chi^{(2)}$ is related to the orientational average of the first molecular hyperpolarizability:

$$\chi^{(2)} = \frac{Nf}{\varepsilon_0} \langle \beta \rangle \quad (1-5)$$

where N is the number density of molecules and f is a ‘‘local field correction’’ to account for the additional electric field arising from the polarization of neighboring molecules.

For the two incident waves of different frequencies ω_1 and ω_2 :

$$\begin{aligned} \mathbf{E}_1 &= \mathbf{E}_1(r) \cos \omega_1 t \\ \mathbf{E}_2 &= \mathbf{E}_2(r) \cos \omega_2 t, \end{aligned} \quad (1-6)$$

$\mathbf{P}^{(2)}$ gives rise to mixing waves of these input fields,

$$\begin{aligned}
\mathbf{P}^{(2)} &= \varepsilon_0 \chi^{(2)} : \mathbf{E}_1 \mathbf{E}_1 + \varepsilon_0 \chi^{(2)} : \mathbf{E}_2 \mathbf{E}_2 + 2\varepsilon_0 \chi^{(2)} : \mathbf{E}_1 \mathbf{E}_2 \\
&= \varepsilon_0 \chi^{(2)} : \mathbf{E}_1(r) \mathbf{E}_1(r) \cos^2 \omega_1 t + \varepsilon_0 \chi^{(2)} : \mathbf{E}_2(r) \mathbf{E}_2(r) \cos^2 \omega_2 t \\
&\quad + 2\varepsilon_0 \chi^{(2)} : \mathbf{E}_1(r) \mathbf{E}_2(r) \cos \omega_1 t \cdot \cos \omega_2 t \\
&= \frac{1}{2} \varepsilon_0 \chi^{(2)} : \mathbf{E}_1(r) \mathbf{E}_1(r) (1 + \cos 2\omega_1 t) + \frac{1}{2} \varepsilon_0 \chi^{(2)} : \mathbf{E}_2(r) \mathbf{E}_2(r) (1 + \cos 2\omega_2 t) \\
&\quad + \varepsilon_0 \chi^{(2)} : \mathbf{E}_1(r) \mathbf{E}_2(r) \{ \cos(\omega_1 + \omega_2) t + \cos(\omega_1 - \omega_2) t \}
\end{aligned} \tag{1-7}$$

The first two terms represent an oscillating polarization at frequencies $2\omega_1$ and $2\omega_2$ together with static polarization. $\mathbf{P}^{(2)}$ also include polarization components which oscillate at the sum and difference frequencies of the two incident waves. The third term is the origins of SFG and difference frequency generation (DFG). In the case of degeneracy, i.e., $\omega_1 = \omega_2$, an SHG signal generates.

The SFG intensity is given by

$$I(\omega_{\text{SF}}) = \frac{8\pi^3 \omega_{\text{SF}}^2 \sec^2 \theta_{\text{SF}}}{c^3} \left| \chi_{\text{eff}}^{(2)} \right|^2 \left| \mathbf{E}_1(\omega_{\text{Vis}}) \mathbf{E}_2(\omega_{\text{IR}}) \right|^2 \tag{1-8}$$

where $\chi_{\text{eff}}^{(2)}$ is the effective nonlinear susceptibility, which takes the form of

$$\chi_{\text{eff}}^{(2)} = [\hat{\mathbf{e}}(\omega_{\text{SF}}) \cdot \mathbf{L}(\omega_{\text{SF}})] \cdot \tilde{\chi}^{(2)} : [\hat{\mathbf{e}}(\omega_{\text{Vis}}) \cdot \mathbf{L}(\omega_{\text{Vis}})] [\hat{\mathbf{e}}(\omega_{\text{IR}}) \cdot \mathbf{L}(\omega_{\text{IR}})] \tag{1-9}$$

with $\hat{\mathbf{e}}(\omega_{\text{SF}})$ being the unit polarization vector and $\mathbf{L}(\omega)$ the tensorial Fresnel factor at frequency ω . The $\chi_{\text{eff}}^{(2)}$ can be expressed as:

$$\chi_{\text{eff}}^{(2)} = \chi_{\text{NR}}^{(2)} + \chi_{\text{R}}^{(2)} \tag{1-10}$$

with

$$\chi_{\text{R}}^{(2)} = N \int \beta(\Omega) f(\Omega) d\Omega \tag{1-11}$$

where Ω represents a set of orientational angles (θ, ϕ, ψ) and $f(\Omega)$ is an orientational distribution function. The $\chi_{\text{NR}}^{(2)}$ and $\chi_{\text{R}}^{(2)}$ are vibrational nonresonant and resonant contributions, respectively. The $\beta_{\text{R}}(\Omega)$ can be written in terms of the sum of the Lorentz functions.

$$\beta_{\text{R}}^{(2)}(\omega_{\text{IR}}, \Omega) = \sum_q \frac{\beta_q}{(\omega_{\text{IR}} - \omega_q) + i\Gamma_q} \tag{1-12}$$

From eq. (1-10), (1-11) and (1-12), we have

$$\chi^{(2)} = \chi_{\text{NR}}^{(2)} + \sum_q \frac{A_q}{(\omega_{\text{IR}} - \omega_q) + i\Gamma_q} \quad (1-13)$$

with

$$A_q = N \int \beta_q(\Omega) f(\Omega) d\Omega. \quad (1-14)$$

Here, β_q , ω_q and Γ_q are the strength, resonant frequency and damping constant of the q th resonant vibrational mode, respectively.

The vibrational resonant SFG process can be considered as a combined process of a resonant IR excitation followed by an anti Stokes Raman process. The quantity β_q in eq. (1-12) can be written in terms of the product of the infrared dipole derivative and the Raman polarizability tensor derivative of the q th vibrational mode, $\partial\mu/\partial Q_q$ and $\partial\alpha/\partial Q_q$, respectively,

$$(\beta_q)_{lmn} \propto \frac{\partial\alpha_{lm}}{\partial Q_q} \frac{\partial\mu_n}{\partial Q_q}, \quad (1-15)$$

where Q_q denotes the q -th normal coordinate, and the subindices (l, m, n) refer to the molecular axis. Within the electric-dipole approximation, the expression for β can be derived from second-order perturbation theory. The general solution is complicated, but reduces to a simpler form if neither ω_{vis} nor ω_{SFG} is resonant with electric transitions in the molecule and only electric dipole transitions are considered. In this case, β is given as:

$$\begin{aligned} & \beta_{lmn}(\omega_{\text{SFG}}, \omega_{\text{vis}}, \omega_{\text{IR}}) \\ &= -\frac{1}{2\hbar} \sum_s \left\{ \frac{\langle g | \mu_l | s \rangle \langle s | \mu_m | v \rangle}{\hbar(\omega_{\text{SFG}} - \omega_{sg})} - \frac{\langle g | \mu_m | s \rangle \langle s | \mu_l | v \rangle}{\hbar(\omega_{\text{vis}} + \omega_{sg})} \right\} \times \left\{ \frac{\langle v | \mu_n | g \rangle}{\omega_{\text{IR}} - \omega_{vg} + i\Gamma_{vg}} \right\} \\ &= -\frac{1}{2\hbar} \sum_s \frac{M_{lm} A_n}{\omega_{\text{IR}} - \omega_{vg} + i\Gamma_{vg}} \end{aligned} \quad (1-16)$$

with

$$M_{lm} = \frac{\langle g | \mu_l | s \rangle \langle s | \mu_m | v \rangle}{\hbar(\omega_{\text{SFG}} - \omega_{sg})} - \frac{\langle g | \mu_m | s \rangle \langle s | \mu_l | v \rangle}{\hbar(\omega_{\text{vis}} + \omega_{sg})} \quad (1-17)$$

$$A_n = \langle v | \mu_n | g \rangle \quad (1-18)$$

where $|g\rangle$ is the ground state, $|v\rangle$ the excited vibrational state, $|s\rangle$ any other state, Γ_{vg} the damping constant, respectively. The quantity M_{lm} can be identified with the Raman scattering tensor which is the Raman polarizability tensor derivative $\partial\alpha/\partial Q$. The term M_{lm} corresponds to a transition between some ground state $|g\rangle$ and an excited vibrational state $|v\rangle$ via a virtual state $|s\rangle$. The quantity A_n is the IR transition dipole moment which is the same as the infrared dipole derivative $\partial\mu/\partial Q$. The term A_n is related to the vibrational transition between $|g\rangle$ and $|v\rangle$. The factor ω_{vg} is the wavenumber of the vibrational transition, ω_{sg} the wavenumber of the transition between the ground state and the virtual state. From the eqs. (1-15) and (1-16), it is evident that an SFG process has to be both Raman and IR active. Also, as the ω_{IR} scans over ω_{vg} , the hyperpolarizability goes through a maximum at $\omega_{IR} = \omega_{vg}$.

A vibrationally resonant SFG signal can be further increased in intensity when the photon energy of the signal is almost the same as one-photon allowed transition energy of the sample (Figure 1.1 (b)). This enhancement can be understood based on equation (1-17). The denominator of the first term becomes very large under the electronic resonant condition ($\omega_{SFG} \approx \omega_{sg}$). SFG in such a condition is called doubly resonant SFG (DR-SFG) [4,16].

As shown above, under the electric dipole approximation, the molecular hyperpolarizability β is a third-rank tensor, and hence the susceptibility χ of a sample that is proportional to the orientationally averaged β is also a third-rank tensor. Therefore, for media with inversion symmetry, SFG is forbidden in the bulk but allowed at the interface. In actuality, the interface contribution does dominate for many interfacial systems. However, the selection rule is only valid under the electric-dipole approximation. It should be pointed out that if we take higher order contributions, the isotropic or even centrosymmetric bulk can in fact contribute to the SFG signal through induced higher-order terms such as electric quadrupole and magnetic dipole [17-19]. The bulk contributions from these terms are not necessarily negligible. Therefore, before the interface selectivity

of the SFG process is exploited, experimental checks must be made to make sure that an SFG signal indeed comes mainly from an interface.

References

- [1] M. Buck and M. Himmelhaus, *J. Vac. Sci. Technol. A* **19**, 2717-2736 (2001).
- [2] Y. R. Shen, *Nature* **337**, 519-525 (1989).
- [3] Y. R. Shen, *Proc. Natl. Acad. Sci. USA* **93**, 12104-12111 (1996).
- [4] M. B. Raschke, M. Hayashi, S. H. Lin, Y. R. Shen, *Chem. Phys. Lett.* **359**, 367-372 (2002).
- [5] A. A. Mari, L. Dreesen, C. Humbert, P. Hollander, Y. Caudano, P. A. Thiry and A. Peremans, *Surf. Sci.* **502-503**, 261-267 (2002).
- [6] X. D. Zhu, H. Suhr, and Y. R. Shen, *Phys. Rev. B* **35**, 3047-3050 (1987).
- [7] D. Wu, G-H Deng, Y. Guo, H-f Wang, *J. Phys. Chem. A* **113**, 6058-6063 (2009).
- [8] M. A. Belkin, Y. R. Shen. *Phys. Rev. Lett.* **91**, 213907 (2003).
- [9] N. Ji, Y. R. Shen, *Chirality*, **18**, 146-158 (2006).
- [10] J. E. Sipe, *J. Opt. Soc. Am. B* **4**, 481-489 (1987).
- [11] V. Mizrahi, J. E. Sipe, *J. Opt. Soc. Am. B* **5**, 660-667 (1988).
- [12] Y. R. Shen, *Annu. Rev. Phys. Chem.* **40**, 327-350 (1989).
- [13] Y. R. Shen, *Surf. Sci.* **299/300**, 551-562 (1994).
- [14] C. D. Bain, *J. Chem. Soc. Faraday Trans.* **91**, 1281-1296 (1995).
- [15] M. Oh-e, H. Yokoyama, D. Kim, *Phys. Rev. E* **69**, 051705 (2004).
- [16] J. Y. Huang, Y. R. Shen, *Phys. Rev. A* **49**, 3973-3981 (1994).
- [17] P.S. Pershan, *Phys. Rev.* **130**, 919-929 (1963).
- [18] E. Adler, *Phys. Rev.* **134**, A728-A733 (1964).
- [19] N. Bloembergen, R. K. Chang, S. S. Jha, C. H. Lee, *Phys. Rev.* **174**, 813-822 (1968).

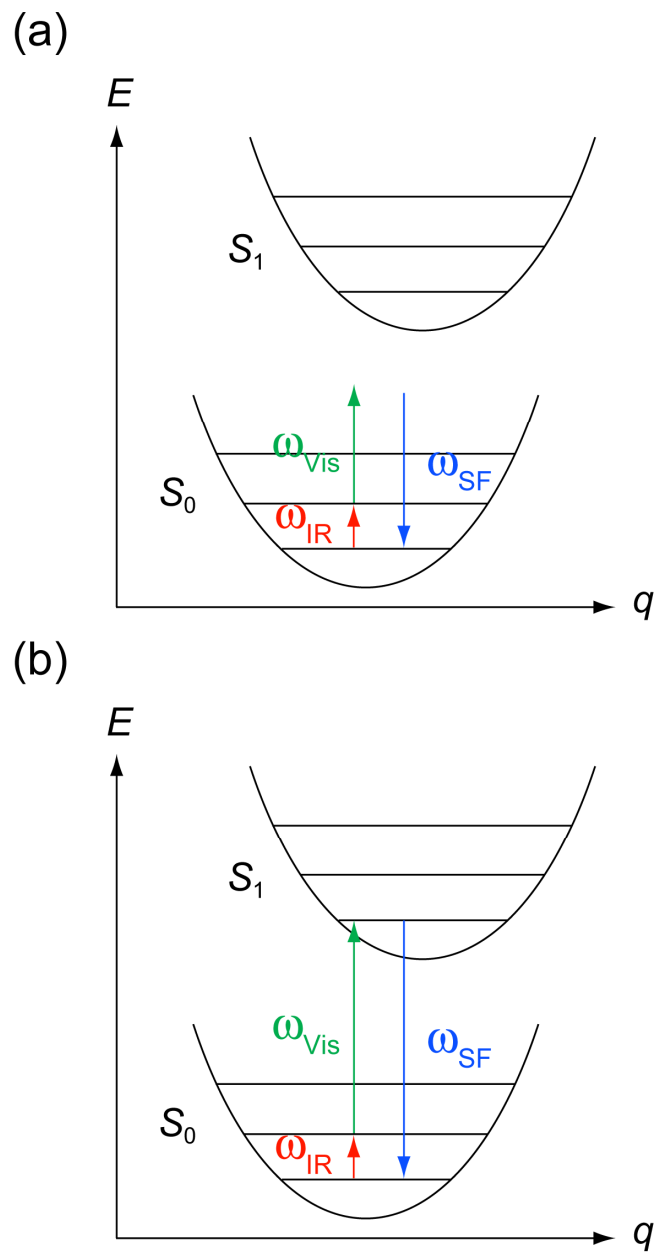


Figure 1.1 Energetic diagram of an SFG process. (a) vibrationally singly resonant SFG (b) vibrationally and electronically doubly-resonant SFG

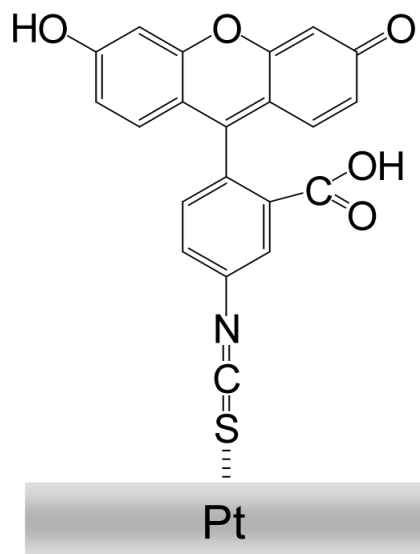


Figure 1.2 neutral fluorescein isothiocyanate isomer-I (FITC) molecule on a platinum surface.

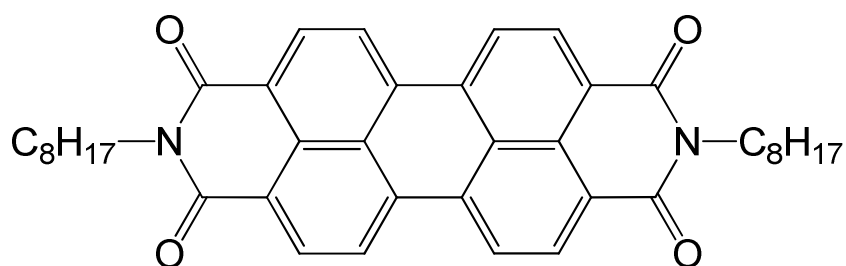


Figure 1.3 Structural formula of N,N'-bis(octyl)perylene-3,4,9,10-tetracarboxylic diimide (PTCDI-C₈)

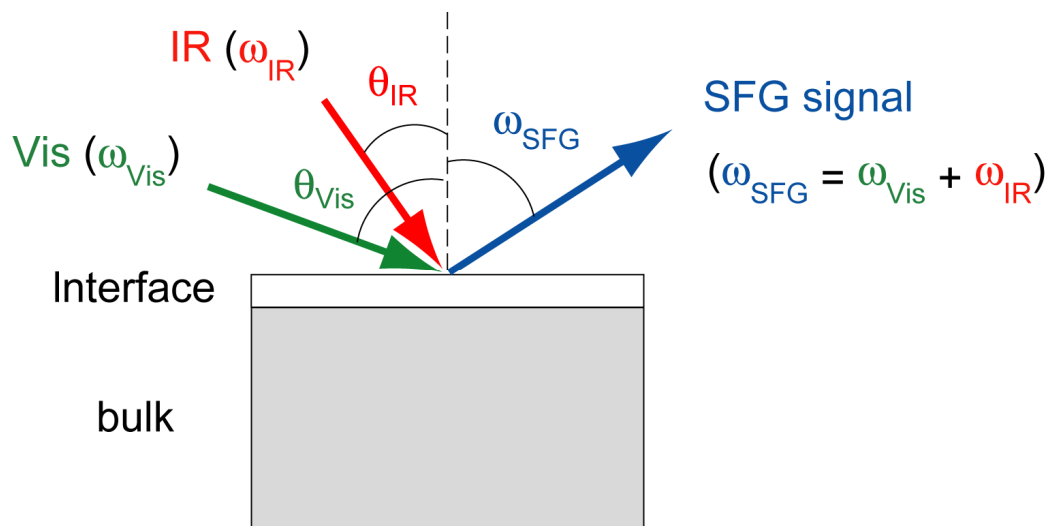


Figure 1.4 Schematic diagram for the generation of an SFG signal. Visible and IR input beams are spatially and temporally incident on a sample.

Chapter 2. Development of an Infrared-Ultraviolet/Visible Sum-Frequency Generation Spectrometer with a Wide Tunability of the Ultraviolet and Visible Probes

2.1 Introduction

To make full use of the doubly resonant effect, it is desirable that the VIS probe wavelength should be as widely tunable as possible. To this end, we have extended the tunable range of the VIS probe to the UV region. The UV-VIS probe of the developed SFG spectroscopy system is tunable in the range of 235-390, 400, and 405-795 nm. The UV extension greatly widens the scope of species to which DRSFG is applicable. Most aromatic molecules and polyenes have electronic absorption bands in the UV region; biological molecules such as aromatic amino acids and nucleobases are included in the widened scope.

In the apparatus, the UV probe was obtained by frequency doubling of a signal output of an optical parametric amplifier (OPA). A prism monochromator was used as a tunable sharp-cut bandpass device to reduce stray light due to the scattering of the UV probe so that any wavelength within the tunable range of the laser system can be chosen as the UV probe wavelength. DR-SFG spectra of a *p*-mercaptobenzoic acid monolayer on gold were measured for the region of 1800-1500 cm^{-1} with 289- and 334-nm UV probes. Two vibrational bands due to the carbonyl stretch and a phenyl ring stretch were observed. Their band intensities observed with the 289-nm probe were approximately three times larger than those with the 334-nm probe, which enhancement has been ascribed to an electronic resonant effect.

2.2 Infrared-Ultraviolet sum-frequency generation spectrometer

The constructed IR-UV SFG apparatus employed a broad-bandwidth (BB), or multiplex SFG method [1]. In this method, the BB SFG signal is generated on a sample from BB IR and narrow-bandwidth (NB) UV probe pulses. The signal is then dispersed spatially by a spectrograph and analyzed with an optical multichannel detector. The BB SFG method offers faster data acquisition than the conventional IR-scanning method, and thus improves the sensitivity of the spectrometer.

The IR-UV SFG apparatus has been developed by extending our IR-VIS multiplex SFG spectrometer [2,3], which has a wide VIS probe tunability in the range of 400 and 470-795 nm. Figure 2.1 schematically depicts the experimental setup. IR and UV probe pulses were obtained by converting the fundamental output (800 nm, 110 fs, 2.5 mJ) of an amplified Ti:Sapphire laser (TITAN II, Quantronix) operated at 1 kHz. One-third of the fundamental output (0.8 mJ) was used to generate the IR probe pulse, while the remaining (1.7 mJ) was used to generate the UV probe pulse.

The IR probe pulse was obtained by difference-frequency mixing in an AgGaS₂ crystal of 0.75 mm thickness between the signal and idler outputs of an optical parametric amplifier (OPA, Light conversion, TOPAS4/800) pumped by the 800-nm output of 0.8 mJ pulse energy. The frequency of the IR pulse was tunable in the range of 3800-1000 cm⁻¹ with pulse energy of 0.4-4 μJ, depending on the IR frequency. The spectral width (FWHM) of the IR probe was typically 200-300 cm⁻¹.

To obtain the UV probe pulse, three frequency conversion steps were performed. In the first step, the femtosecond fundamental pulse of an 800-nm wavelength was converted to a picosecond NB 400-nm pulse by using sum-frequency mixing of phase-conjugated picosecond pulses, which were prepared by stretching the femtosecond input pulse [3,4]. The generated 400-nm pulse had a pulse duration of 5 ps and a full width at half maximum (FWHM) of 8 cm⁻¹. The output energy of 450 μJ was obtained from 1.7 mJ of the fundamental input, corresponding to a conversion efficiency of 26%. In the second step,

the 400-nm pulse pumped the other OPA (Light Conversion, TOPAS4/400) to generate a visible pulse as the signal output, which was frequency tunable in the range of 470-795 nm. Visible probe wavelengths of 405-500 nm can be applicable as the second harmonic of the idler output. The pulse energy of the signal varied from 20 to 60 μJ , depending on its wavelength. The bandwidth of the signal was 8-10 cm^{-1} . In the final step, the signal output was converted to a UV probe pulse by second harmonic generation in a 3-mm-thick $\beta\text{-BaB}_2\text{O}_4$ (BBO) crystal. The UV pulse was separated from the signal outputs using a visible light cut filter (SIGMA KOKI, UTVAF-33U). The separated pulse was used as the UV probe for SFG spectroscopy. The UV probe tunable range in which more than 1 μJ pulse energy was obtainable was from 235 to 390 nm. The FWHM of the UV probe was typically about 10 cm^{-1} .

The IR and UV probe beams thus obtained were spatially and temporally overlapped on a sample surface with incidence angles of 50° and 70° from the surface normal of the sample, respectively. The UV and IR probes were p-polarized. The IR beam was focused with a 10-cm focal-length (FL) CaF_2 lens and the UV beam with a 20-cm FL SiO_2 lens. The SFG signal generated in the reflected direction was collimated by a 10-cm FL SiO_2 lens, separated from the reflected UV probe with a diameter-adjustable circular aperture, and then focused on the entrance slit of a spectrograph by a 10-cm FL SiO_2 lens. The signal was dispersed spatially with the spectrograph and detected with a UV-sensitive back-illuminated charge-coupled device (CCD) detector (Roper Scientific, LN LN/CCD-1340/400-EB).

Stray light due to scattered UV probe light is generally problematic in detecting the SFG signal because the signal is very weak compared to probe light. To suppress stray light, conventional SFG spectrometers use plate-shape optical filters that transmit the SFG signal light but block the UV/VIS probe light. This method is simple and very effective. However, if the UV/VIS probe is tunable, a separate filter is needed for each probe wavelength. Moreover, appropriate plate-shape filters may be difficult to obtain in the UV

region compared to the VIS region, in which good quality filters, such as notch-filters for Raman spectroscopy [5], are available. In our set up, we used a prism monochromator as a wavelength-variable sharp cut filter to suppress stray light.

The spectrograph consisted of an F/6 200-mm prism monochromator (Jasco, CT-25UV) and an F/6.4 550-mm grating polychromator (HORIBA Jobin-Yvon, TRIAX-550). A schematic diagram of the spectrograph is shown in Figure 2.2. This configuration of the spectrograph has been demonstrated to offer at the same time a high throughput and a low stray light level in UV Raman spectroscopy [6], in which detection of a weak signal frequency-shifted from the Raman excitation probe is required as in SFG spectroscopy. In the spectrograph, the incident SFG signal was weakly dispersed by a prism (fused silica, Littrow-type with 30° apex angle, backside coated with aluminum) after being collimated by a concave mirror (CM2), and then it was focused on the plane of the second slit (S2). The SFG signal went through S2 and entered into the main polychromator stage, while scattered UV probe light was blocked by S2; consequently, the stray-light due to the probe was greatly reduced. In the main polychromator, the transmitted light was then collimated again, dispersed further by the grating (HORIBA Jobin Yvon, 4320-groves/mm holographic), and refocused on the CCD detector. The prism in the first stage and the grating in the second stage were coupled so that their dispersions were subtractive. The reciprocal linear dispersion of the prism stage was much smaller than that of the grating stage. For instance, the reciprocal linear dispersion of the prism stage of 7.1 nm/mm (930 cm⁻¹/mm) was about 20 times larger than that of the grating stage which is 0.42 nm/mm (54 cm⁻¹/mm) at 280 nm. The total dispersion of the spectrograph was, therefore, mainly due to the grating stage.

The reflectivity of the prism was evaluated using emission lines from a low-pressure mercury lamp (UVP, Inc, Pen-Ray). The prism can be replaced with an aluminum flat mirror coated with MgF₂. With the mirror instead of the prism, the image of the entrance slit (S1) is not dispersed but just transferred to the center of the second slit

(S2). The area intensities of eight emission lines from mercury (229, 239, 267, 277, 291, 298, 315, and 367 nm) were measured with the prism and with the mirror. From the ratios between the intensities with the prism and those with the mirror, we evaluated the reflectivity of the prism relative to the aluminum mirror. The averaged reflectivity of the prism was 86% for the eight measured lines. All the mirrors in the prism stage were aluminum coated with MgF₂. Assuming aluminum mirrors reflect 90% of incoming UV light, the total throughput of the first stage of the spectrograph was estimated as 56%, for the stage consists of three aluminum coated mirrors and the prism. Such a high throughput over the wide wavelength range of UV light could not be realized with a grating instead of a prism as the dispersing element of the first stage.

The stray light rejection efficiency by the first prism stage was estimated and found to be high enough to record SFG spectra with a low stray-light level. To estimate the efficiency, SFG signals from a GaAs (110) substrate measured with the prism in the first stage were compared with those measured with the mirror instead of the prism. The signal obtained with the mirror was expected to simulate a signal measurable with a simple single polychromator without pre-filtering scattered probe light.

Figure 2.3 shows the data measured with the prism in the first stage. The UV probe wavelength was 289 nm, and the widths of S1 and S2 were 100 μm and 900 μm , respectively. SFG signals from the GaAs substrate were identified as a broad peak centered at around 1700 cm^{-1} on the spectra (A1, B1, C1, and D1 in Figure 2.3). A1, B1, C1, and D1 spectra were recorded with the sizes of the aperture (see Figure 2.1) of 6, 7, 8, and 9 mm, respectively. The aperture was installed to block the direct reflection of probe beams from the sample surface. By changing the aperture size, we can control the stray light level of the sample.

The observed spectra were due to a vibrationally non-resonant contribution of the GaAs substrate, and had a single peak. The spectral shape was primarily determined by the IR probe spectra. The intensity below 1400 cm^{-1} slightly was increased with an

increase of the diameter of the circular aperture. The extra signals observed with larger aperture diameters (8 and 9 mm) were stray light due to scattered UV probe light because they persisted without the IR probe (C2 and D2 in Figure 2.3). A2, B2, C2, and D2 spectra (dotted lines) were measured without the IR probe, and correspond to the stray light with the aperture diameters of 6, 7, 8, and 9 mm, respectively. The stray light was not recognized with an aperture of 6-mm diameter, by which almost the whole reflected UV probe beam was blocked. Small but detectable stray light was clearly observed when the aperture diameter increased to 9 mm. The 9-mm diameter aperture blocked half of the reflected UV probe beam.

Spectra were severely distorted by stray light when measured with the mirror installed instead of the prism in the first stage of the spectrograph. Spectra were overwhelmed by stray light, and the SFG signal could not be identified when the aperture diameter was increased to 7 mm or larger (Figure 2.4B-2.4D). With a 6-mm aperture, the SFG signal and a false signal due to stray light were comparable (Figure 2.4A). The stray-light rejection efficiency of the first stage with the prism was estimated to be 99.96% by comparing the intensity of stray light in Figure 2.3D with that in Figure 2.4D.

It is important to mention that the GaAs substrate had a smooth, mirror-finished surface and a large SFG susceptibility; therefore it displayed a smaller scattering of the UV probe and a much stronger SFG signal than that from an ordinary organic monolayer. It may be difficult to detect the SFG signal from ordinary organic films if a single polychromator is used without any spectrally pre-filtering of scattered UV probe by some optical filter, either a monochromator or a plate-shape filter.

2.3 Infrared-Ultraviolet sum-frequency generation spectra of a *p*-mercaptobenzoic acid monolayer on gold

We measured IR-UV SFG spectra of a *p*-mercaptobenzoic acid (*p*-COOHC₆H₄SH) monolayer on gold with the ppp (from the left character, p-polarized sum-frequency output, p-polarized visible input, p-polarized IR input, respectively) polarization combination. We selected the sample because the adsorbate is one of the most typical aromatic molecules and the monolayer is easy to prepare [7]. In this study, we focused on demonstrating the feasibility of the DR-SFG measurements in the UV region, not selective detection of adsorbates by an electronic resonance. The monolayer was prepared by immersing a gold substrate (Molecular Imaging Picosubstrate) in a 1 mM ethanol solution of *p*-mercaptobenzoic acid (Kanto Kagaku, > 99.5%) for about 24 hours. The UV absorption spectrum of the ethanol solution (0.5 mM) of *p*-mercaptobenzoic acid is shown in Figure 2.5A. The molecule has an allowed electronic transition at around 280 nm with a molar absorption coefficient of 16000 mol⁻¹dm³cm⁻¹. Since we could not measure the absorption spectrum of the monolayer, with reference to the ethanol solution spectrum, we chose two UV probe wavelengths of 289 nm, expecting exact resonance, and 334 nm pre-resonance. The wavelengths of the SFG signal with a 1600 cm⁻¹ shift are 276 and 317 nm for the 289- and 334-nm probes, respectively. Figure 2.6 shows the SFG spectra of the monolayer measured with these two UV probes. The intensities of the spectra were normalized by dividing them by SFG spectra of the Y-cut quartz measured with the same UV and IR probes. SFG susceptibility of the quartz is expected to be approximately the same for the 289- and 334-nm UV probes because it is transparent for the light whose wavelength is longer than 200 nm.

A sharp vibrational band at 1587 cm⁻¹ and a broad band at around 1724 cm⁻¹ were identified on both spectra. The former band was due to phenyl stretch, and the latter to carbonyl stretch. These two vibrations were observed at 1589 and 1749 cm⁻¹ by infrared reflection-absorption spectroscopy (IRAS) [7]. The positions of the phenyl band agreed

well between SFG and IRAS spectra, but those of the carbonyl band differed slightly. The carbonyl stretch band of the IRAS spectrum was a very broad (FWHM $\sim 40 \text{ cm}^{-1}$) asymmetric band having its peak at 1749 cm^{-1} , while the corresponding SFG band was observed at 1724 cm^{-1} with a broad (FWHM $\sim 40 \text{ cm}^{-1}$) symmetric band shape. The reason for this difference is not clear. The quality of a monolayer may affect the carbonyl band position, which depends on the degree of hydrogen bonding and therefore is sensitive to aggregation of adsorbate and adsorption of water from ambient.

It is noted that the vibrationally nonresonant background signals were very small for both of the observed IR-UV SFG spectra. This is in contrast to the rather large nonresonant signal from gold for IR-VIS SFG. The small nonresonant signal for IR-UV SFG can be understood if the probe frequency dependence of the nonresonant signal of gold in the visible region is extrapolated. When the IR probe frequency is 2900 cm^{-1} , the nonresonant SFG signal from gold exhibited a peak at the VIS probe frequency of 19000 cm^{-1} (536 nm), decreased with the VIS probe frequency, and became 15 times smaller with a 25000 cm^{-1} (400 nm) probe than its peak value [2].

The normalized band intensities of the SFG spectra of the monolayer depended on the UV probe wavelength. The band intensities measured with the 289-nm probe were about three times larger than those measured with the 334-nm probe. To quantitatively evaluate the band intensity ratio between the two spectra, the observed spectra were analyzed by a least-squares fitting. The model function was the square of the modulus of effective SFG susceptibility χ_{eff} , which is a sum of a constant and Lorentz functions [8]:

$$\chi_{\text{eff}} = A_{\text{NR}} + \sum_{q=1}^2 \frac{A_q \exp(i\phi_q)}{\omega_q - \omega_{\text{IR}} - i\Gamma_q} \quad (2-1)$$

where ω_{IR} is the wavenumber of the IR probe; A_{NR} is the amplitude of the vibrationally nonresonant contribution by the substrate, A_q , ω_q , Γ_q , and ϕ_q are the amplitude, resonant wavenumber, damping constant, and relative phase of the q -th vibrational mode of the adsorbate, respectively. The phases of the two vibrational bands, ϕ_q s, were indeterminable

because A_{NR} was small compared to the amplitudes of vibrational terms A_{qs} . We assumed that the phases of the two vibrational bands are both equal to zero. The estimated parameters are listed in Table 1. Errors (numbers following \pm symbol) in the table are standard deviations of the parameters. The ratios between the amplitude with the 289-nm probe and the 334-nm probe were 1.7 ± 0.1 and 1.8 ± 0.2 for the phenyl band and the carbonyl band, respectively.

The effective SFG susceptibility χ_{eff} can be expressed in terms of Cartesian components of SFG susceptibility and the Fresnel coefficients. The Fresnel coefficients depend on the UV-probe wavelength. The variation of the coefficients for the 289- and 334-nm UV probes is a possible reason for the observed UV probe dependence of the SFG band intensities. However we found that the variation was too small to explain the observed band intensity variations of about 3. The sample was uniaxial, and UV and IR probes were both p-polarized. Under this condition, the effective susceptibility can be expressed as follows [9]:

$$\begin{aligned}
\chi_{\text{eff}} = & -L_{xx}(\omega_{\text{SFG}})L_{xx}(\omega_{\text{UV}})L_{zz}(\omega_{\text{IR}})\cos\beta_{\text{SFG}}\cos\beta_{\text{UV}}\sin\beta_{\text{IR}}\chi_{xxz} \\
& -L_{xx}(\omega_{\text{SFG}})L_{zz}(\omega_{\text{UV}})L_{xx}(\omega_{\text{IR}})\cos\beta_{\text{SFG}}\sin\beta_{\text{UV}}\cos\beta_{\text{IR}}\chi_{xzx} \\
& +L_{zz}(\omega_{\text{SFG}})L_{xx}(\omega_{\text{UV}})L_{xx}(\omega_{\text{IR}})\sin\beta_{\text{SFG}}\cos\beta_{\text{UV}}\cos\beta_{\text{IR}}\chi_{zxx} \\
& +L_{zz}(\omega_{\text{SFG}})L_{zz}(\omega_{\text{UV}})L_{zz}(\omega_{\text{IR}})\sin\beta_{\text{SFG}}\sin\beta_{\text{UV}}\sin\beta_{\text{IR}}\chi_{zzz}
\end{aligned} \tag{2-2}$$

where xyz is the Cartesian coordinate system chosen so that z is parallel to the surface normal of the sample, and the probe beams lie on the xz -plane. χ_{ijk} ($i, j, k = x, y, \text{ or } z$) are Cartesian components of SFG susceptibility; $L_{ii}(\omega)$ ($i = x, y, \text{ or } z$) are the Fresnel coefficients for beams whose frequency is ω ; and β_{SFG} , β_{UV} , and β_{IR} are the angles between the surface normal and the SFG, UV probe, and IR probe beams, respectively. $L_{xx}(\omega_{\text{IR}})$ is much smaller than $L_{zz}(\omega_{\text{IR}})$ because the substrate is gold. Therefore, only two factors in equation 2-2, $L_{zz}(\omega_{\text{SF}})L_{zz}(\omega_{\text{UV}})L_{zz}(\omega_{\text{IR}})$ and $L_{xx}(\omega_{\text{SF}})L_{xx}(\omega_{\text{UV}})L_{zz}(\omega_{\text{IR}})$, need to be considered. We calculated Fresnel coefficients [10] using the literature values of the complex refractive index of gold [11]. $|L_{zz}(\omega_{\text{SF}})L_{zz}(\omega_{\text{UV}})L_{zz}(\omega_{\text{IR}})|^2$ for the 289-nm probe was 0.93 times

larger than that for the 334-nm probe, and for the 289 nm probe $|L_{xx}(\omega_{\text{SF}})L_{xx}(\omega_{\text{UV}})L_{zz}(\omega_{\text{IR}})|^2$ was 1.11 times larger than that for the 334-nm probe. The variation of the square of the factors are smaller than the observed variation of the SFG band intensity, hence the former cannot be responsible for the latter.

The enhancement of the vibrational SFG band amplitude is probably due to electronic resonance with the allowed absorption of *p*-mercaptobenzoic acid. However, it was not as large as expected from the absorption spectrum of the ethanol solution. We think that this quantitative discrepancy was due to the difference between the UV absorption of the monolayer and that of the ethanol solution. It is not unusual that the position and width of an electronic absorption band of a chromophore largely depends on whether it is on a substrate or in solution. A spin-coated film of *p*-mercaptobenzoic acid on a silica substrate displayed electronic absorption bands that were broadened and red-shifted compared to those of the ethanol solution (Figure 2.5B). One of the probable reasons for the change in the absorption bands is the change in intermolecular interaction; the interaction between the aromatic adsorbates is important on the monolayer whereas the solvent-solute interaction is crucial for the solution. In addition to the intermolecular interaction between the aromatic adsorbates, the interaction between the adsorbate and the metal substrate through the S-Au bond can further perturb the electronic states of the adsorbate for the monolayer on Au. Therefore, it is most likely that the spectrum of the monolayer sample differs substantially from that of the ethanol solution. To evaluate this idea, we need to measure the UV probe frequency dependence of SFG spectrum of the monolayer in more detail. A study along this line is now in progress.

2.4 Conclusion

We have developed a multiplex IR-UV/visible SFG spectrometer with a wide tunability range of 235–390, 400, 405–795 nm. As long as we know, this is the first spectrometer in which a multiplex method is adopted and a UV probe can be used. To reduce the stray light due to scattered UV and VIS probes, a prism monochromator was used as a tunable sharp-cut bandpass device. For a test measurement of IR-UV DR-SFG, a *p*-mercaptobenzoic acid monolayer on a gold substrate was measured. The intensity enhancements of vibrational SFG bands by electronic resonance effect were observed for a *p*-mercaptobenzoic acid monolayer in the UV region. The UV extension of the probe broadens the scope of DR-SFG to almost all aromatic molecules, which include biologically important nucleobases (purine, pyrimidine) and aromatic amino acids.

References

- [1] L. J. Richter, T. P. Petralli-Mallow, and J. C. Stephenson, *Opt. Lett.* **23**, 1594-1596 (1998).
- [2] T. Ishibashi and H. Onishi, *Appl. Phys. Lett.* **81**, 1338-1340 (2002).
- [3] T. Ishibashi and H. Onishi, *Appl. Spectrsc.* **56**, 1298-1302 (2002).
- [4] F. Raoult, A. C. L. Boscheron, D. Husson, C. Sauteret, A. Modena, V. Malka, F. Dorchies, and A. Migus, *Opt. Lett.* **23**, 1117-1119 (1998).
- [5] M. M. Carrabba, K. M. Spencer, C. Rich, and D. Rauh, *Appl. Spectrsc.* **44**, 1558-1561 (1990).
- [6] S. Hashimoto, T. Ikeda, H. Takeuchi, and I. Harada, *Appl. Spectrsc.* **47**, 1283-1285 (1993).
- [7] S. E. Creager and C. M. Steiger, *Langmuir* **11**, 1852-1854 (1995).
- [8] Y. R. Shen, *Proc. Natl. Acad. Sci. USA* **93**, 12104-12111 (1996).
- [9] X. Zhuang, P. B. Miranda, D. Kim, and Y. R. Shen, *Phys. Rev. B* **59**, 12632-12640 (1999).
- [10] E. D. Palik, Ed., *Handbook of Optical Constants of Solids* (Academic Press, New York, 1985).
- [11] T. Ishibashi, H. Uetsuka, and H. Onishi, *J. Phys. Chem. B* **108**, 17166-17170 (2004).

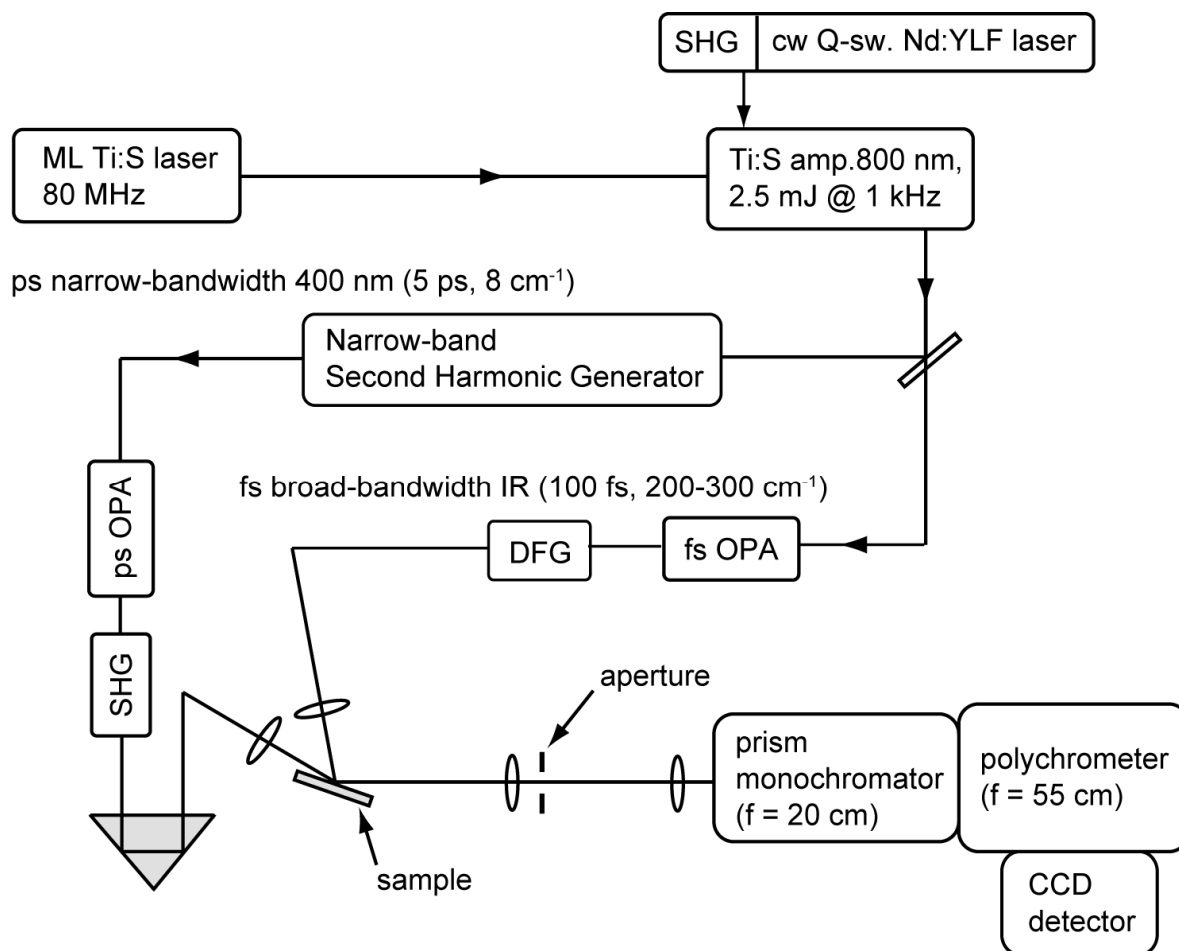


Figure 2.1 Block diagram of the multiplex IR-UV SFG spectrometer

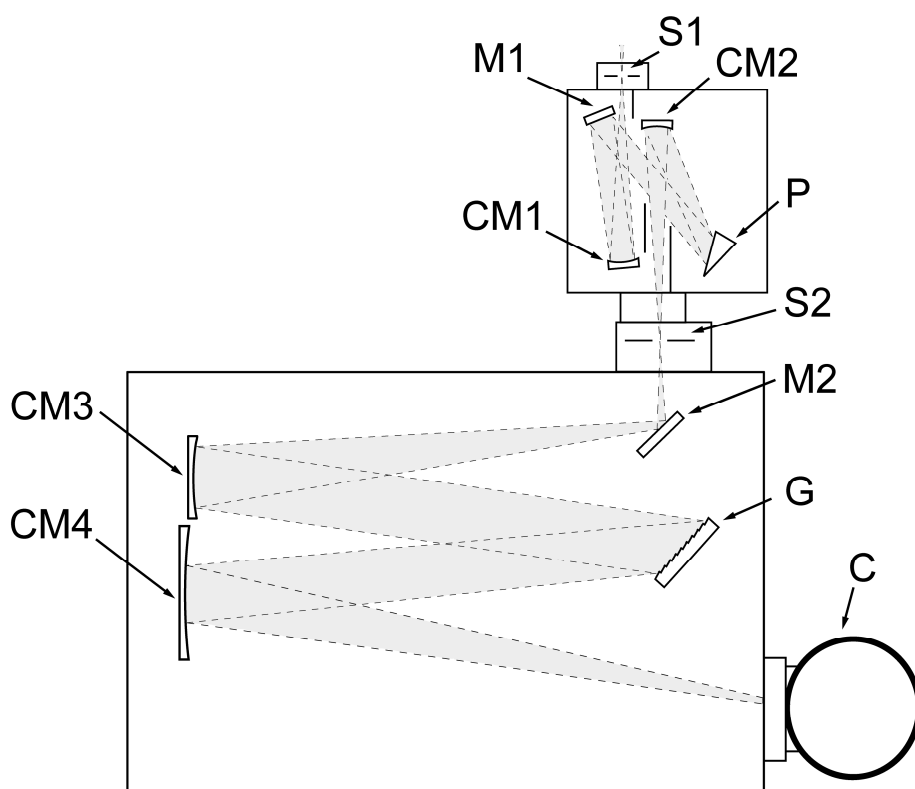


Figure 2.2 Schematic view of the spectrograph for IR-UV SFG spectroscopy.

S1: entrance slit; S2: second slit; CM1, CM2, CM3, CM4: concave mirrors; M1, M2: flat mirrors; C: CCD detector; P: prism(fused silica, Littrow-type with 30° apex angle, backside coated with aluminum); G: grating (4320 grooves/mm).

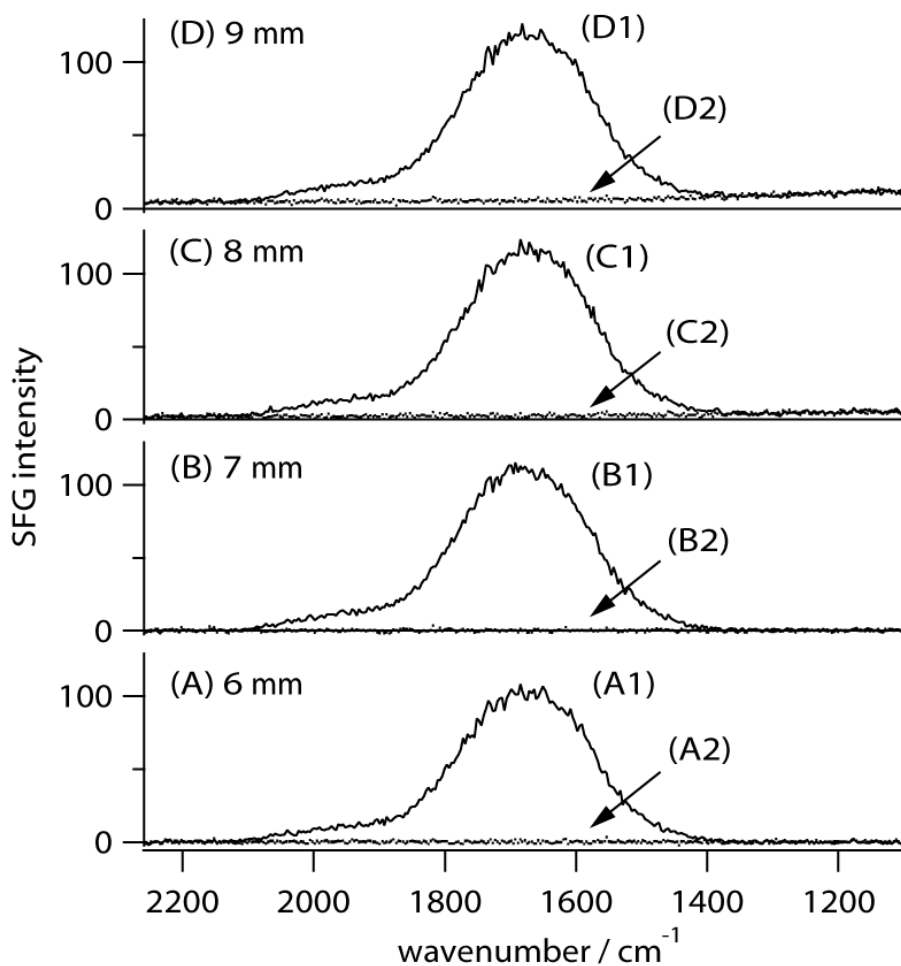


Figure 2.3 SFG signal from GaAs (110) measured with the spectrograph with a prism installed.

Solid lines (A1, B1, C1, D1) indicate measurements with IR and UV probes. Dotted lines (A2, B2, C2, D2) indicate stray light measured with UV probe only. The UV probe wavelength was 289 nm. The aperture diameters were A1 and A2: 6, B1 and B2: 7, C1 and C2: 8, and D1 and D2: 9 mm.

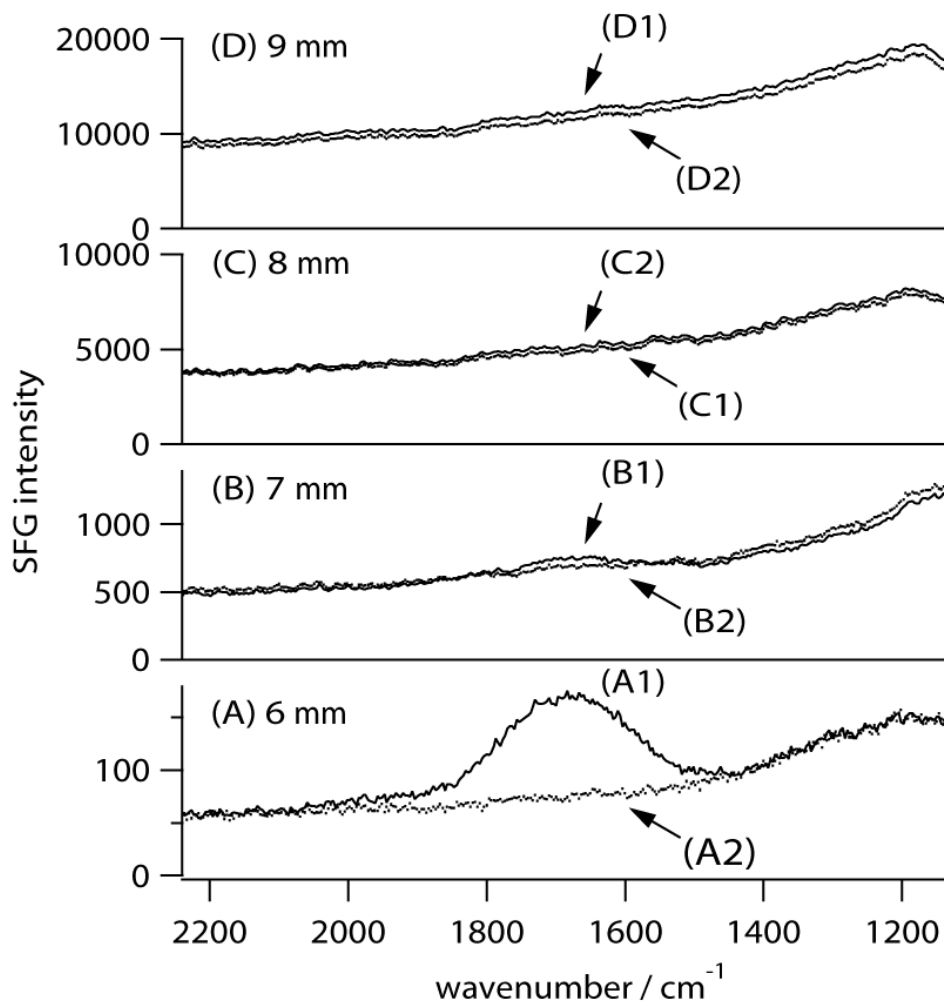


Figure 2.4 SFG signal from GaAs (110) measure with the spectrograph with a mirror installed instead of a prism.

Solid lines (A1, B1, C1, D1) indicate measurements with IR and UV probes. Dotted lines (A2, B2, C2, D2) indicate stray light measured with UV probe only. The UV probe wavelength was 289 nm. The aperture diameters were A: 6, B: 7, C: 8, and D: 9 mm.

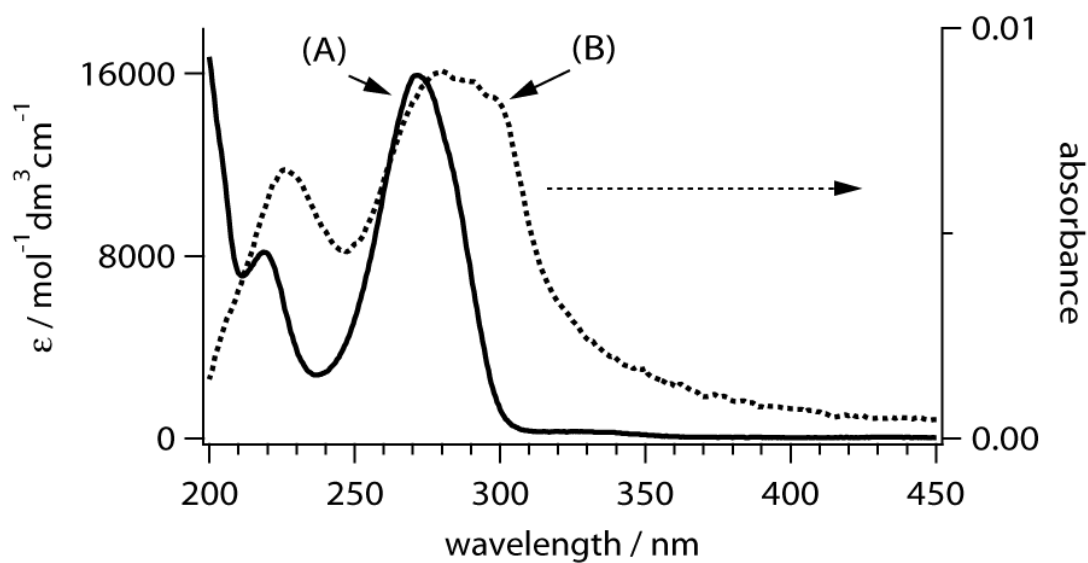


Figure 2.5 UV-visible absorption spectrum of ethanol solution and a spin-coated film of *p*-mercaptobenzoic acid.

(A) Solid line indicates the absorption spectrum of *p*-mercaptobenzoic acid in ethanol (0.5 mM), (B) dotted line indicates the absorption spectrum of *p*-mercaptobenzoic acid monolayer on a SiO₂ substrate.

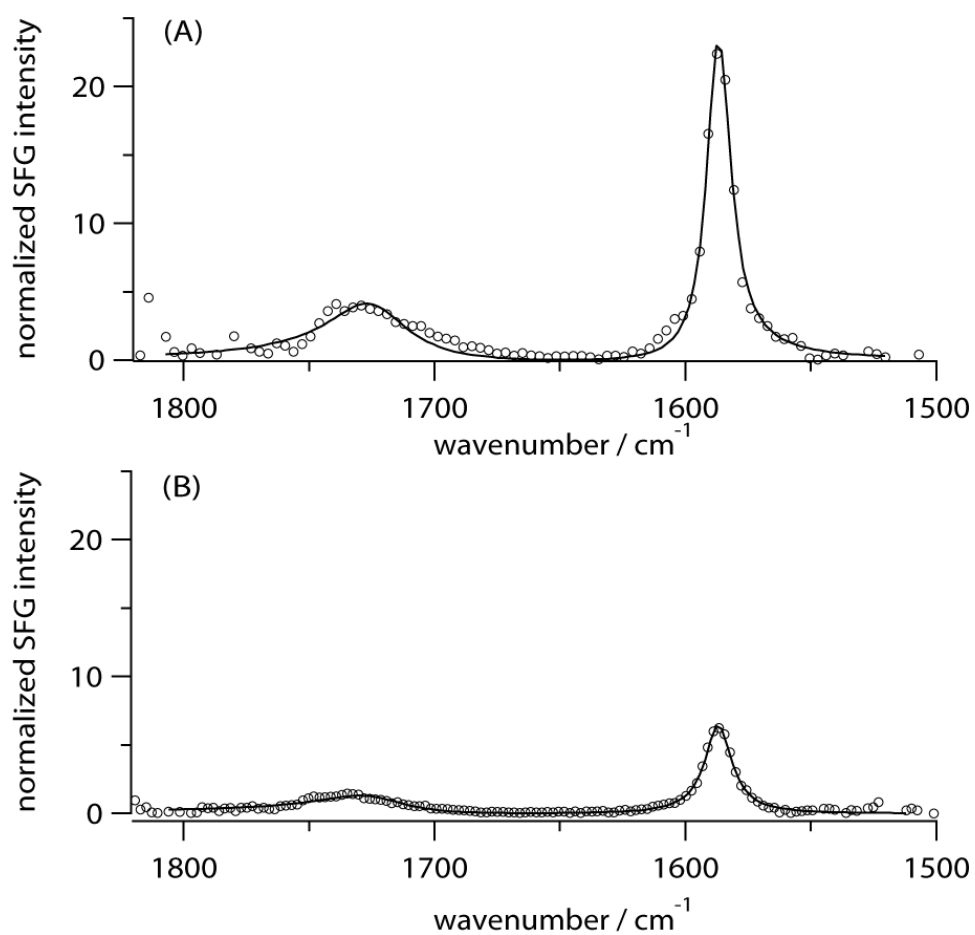


Figure 2.6 IR-UV SFG spectra of a *p*-mercaptobenzoic monolayer on gold. (A) UV probe: 289 nm, UV probe pulse energy: 0.11 μJ , IR probe pulse energy: 2.2 μJ , exposure time: 200 sec; (B) UV probe: 334 nm, UV probe pulse energy: 0.15 μJ , IR probe pulse energy: 2.5 μJ , exposure time: 200 sec. Circles are observed data and solid lines are fitting results to eq. (1).

| | | UV probe wavelength / nm | |
|---------------------|-----------------------------|--------------------------|------------------|
| | | 289 | 334 |
| Nonresononant term | A_{NR} | -0.07 ± 0.04 | -0.17 ± 0.02 |
| C=O stretch | $\omega_q / \text{cm}^{-1}$ | 1724 ± 1 | 1724 ± 1 |
| | A_q | 40 ± 3 | 23 ± 1 |
| | $\Gamma_q / \text{cm}^{-1}$ | 20 ± 2 | 22 ± 1 |
| | ϕ_q | 0 (fixed) | 0 (fixed) |
| Phenyl ring stretch | $\omega_q / \text{cm}^{-1}$ | 1587 ± 0.2 | 1587 ± 0.2 |
| | A_q | 28.1 ± 0.6 | 16.5 ± 0.3 |
| | $\Gamma_q / \text{cm}^{-1}$ | 5.9 ± 0.2 | 6.5 ± 0.2 |
| | ϕ_q | 0 (fixed) | 0 (fixed) |

Table 1. Band parameters of IR-UV SFG spectra of *p*-mercaptobenzoic acid (*p*-HOOC-C₆H₄-SH) monolayer on gold

Chapter 3. Chemical Species of Fluorescein Isothiocyanate Isomer-I (FITC) Monolayers on Platinum Probed by Doubly Resonant Sum-Frequency Generation Spectroscopy

3.1 Introduction

As described in general introduction, DR-SFG can be applied to identify several chemical species on the same substrate by measuring DR-SFG excitation profiles for some vibrational bands. To demonstrate this advantage, fluorescein isothiocyanate isomer-I (FITC) monolayer on platinum (Figure 1.1) has been studied by DR-SFG.

FITC (Figure 3.1) is a representative derivative of fluorescein and widely used in bioscience as a fluorescent labeling reagent for proteins [1,2] and as a reagent in the fluorescent antibody technique for rapid identification of pathogens [3,4]. The versatility of FITC is based on its large molar extinction coefficient and high fluorescent quantum yield. The fluorescein chromophore in aqueous solutions is well known to take several protolytic forms (cation, neutral, anion, and dianion), which makes the electronic spectra of the solutions remarkably dependent on their pH [5]. However, the protolytic forms of FITC when chemisorbing on metal substrates are not known. We applied vibrationally-electronically doubly resonant sum-frequency generation (DR-SFG) spectroscopy to analyze the chemical species of FITC monolayers on platinum substrates.

We have conducted measurements of DR-SFG spectra of the FITC monolayers and found that there were two vibrational bands that exhibited distinct DR-SFG excitation profiles. An alkaline treatment of the sample revealed that the difference was due to two co-existing protolytic forms of FITC on the substrate. Assignments of the forms were proposed by comparison between the DR-SFG excitation profiles and the electronic absorption spectra of fluorescein in aqueous solutions.

3.2 Experimental

The details of the spectrometer have been described in Chapter 2. The important point was shown here. Our spectrograph consisted of a prism monochromator and a grating single polychromator. This kind of composite spectrograph was required to suppress unwanted stray light due to the scattering of the VIS probe and measure weak SFG signals. A prism made of S-BSM2 glass (Littrow-type with 30° apex angle, backside coated with aluminum) was used in the prism monochromator and a 2400-grooves/mm holographic grating with 330-nm blazed wavelength in the grating polychromator. The reciprocal linear dispersion of the prism stage was 26 nm/mm (1000 cm⁻¹/mm) at 500 nm.

Fluorescence and fluorescence excitation spectra of the monolayers were measured with a conventional fluorescence spectrometer (F-2500, Hitachi).

FITC monolayers were formed on platinum substrates (a 200-nm thick film on glass, Koshin Kogaku) by immersing the substrates in a 1 mM ethanol solution of FITC (Dojin Kagaku) for about 24 hours. In order to minimize contamination, the substrates were cleaned by placing in a chromic acid solution (Wako Pure Chemical) for about 24 hours, which strongly oxidizes organic contaminants, and then rinsed with ultrapure water (resistance > 1.8×10⁵ Ω m) and ethanol. Immediately after the cleaning, they were immersed into the ethanol solution of FITC for about 24 hours for deposition. After being removed from the solution, the substrate was rinsed thoroughly with copious ethanol and was dried in a flow of nitrogen gas for the purpose of removing physisorbed FITC molecules.

3.3 Vibrational SFG spectra and DR-SFG excitation profiles of FITC monolayers on platinum

Vibrational SFG spectra of an FITC monolayer on a platinum substrate were measured with six probe wavelengths (434, 453, 480, 536, 558, and 581 nm) under the ppp polarization combination. The observed spectra are shown in Figure 3.2 (L1-L6). The SFG intensities shown were normalized against that of Y-cut quartz measured with the same VIS and IR probes. SFG susceptibility of the quartz is expected to be approximately constant in the visible region because it is transparent for the visible light.

A strong vibrational band was observed at around 1640 cm^{-1} in all the six spectra, and the band intensity increased when the VIS probe wavelength was changed from 434 to 536 nm, and it then decreased from 536 to 581 nm. The VIS probe wavelength dependence clearly showed that the vibrational SFG band intensity was enhanced by electronic resonance due to an absorption band of FITC in the visible region. The 1640-cm^{-1} band is probably assigned to a stretch mode of xanthene group in FITC.

The spectral shape as well as the intensity varied with the visible probe wavelength. This was because there were two vibrational bands in the IR wavenumber region of $1700\text{-}1600 \text{ cm}^{-1}$. The observed spectra, $I_{\text{SFG}}(\omega_{\text{IR}})$, were successfully reproduced by using the standard model function. The model function is the square of the modulus of the effective SFG susceptibility χ_{eff} , which is a sum of a constant and Lorentz functions [6]

$$I_{\text{SFG}}(\omega_{\text{IR}}) = |\chi_{\text{eff}}(\omega_{\text{IR}})|^2, \quad (3-1)$$

$$\chi_{\text{eff}}(\omega_{\text{IR}}) = A_{\text{NR}} + \sum_{q=1}^2 \frac{A_q \exp(i\phi_q)}{\Omega_q - \omega_{\text{IR}} - i\Gamma_q},$$

where A_{NR} denotes the amplitude of vibrationally nonresonant term, and A_q , Ω_q , Γ_q , and ϕ_q refer to the amplitude, resonant wavenumber, damping constant, and phase of the q -th

resonant vibrational mode, respectively. The results of the simulation are shown as lines in Figure 3.2. In the simulation, we assumed that the resonant wavenumbers and bandwidths of the two bands were in common in the six SFG spectra. The determined resonant wavenumbers were 1643 and 1610 cm^{-1} . In the following, we refer to the larger wavenumber band at 1643 cm^{-1} as band A, and the smaller wavenumber one at 1610 cm^{-1} as band B.

The SFG excitation profiles for the vibrational bands A and B are shown in Figure 3.3 as (a) and (b), respectively. The excitation profiles were constructed by plotting of the amplitude, A_q , of each band as a function of the SFG wavelength. The shapes of the two SFG excitation profiles were significantly different from each other. The excitation profile for band B has its peak at a shorter wavelength and narrower bandwidth than for band A.

There are several possible reasons for the difference between the excitation profiles of band A and band B. The first is the different structural changes of the resonant excited state along the two vibrational modes, compared to the electronic ground state. The SFG excitation profiles mainly depend on the corresponding linear absorption spectrum, but it also depends on the structural changes [7]. The excitation profiles of the two modes can be largely different if the changes along the two modes are largely different. However, all excitation profiles observed thus far are not markedly different from the corresponding linear absorption spectrum [7,8]. Another possible reason is that different electronic states contribute to the electronic enhancements of the two bands. This possibility can be divided into two cases. The first one is that the different resonances are due to different electronic states of a single chemical species. The second one is that different chemical species co-existing in the sample correspond to the two bands.

We performed an alkaline treatment of the sample and concluded that two different chemical forms of FITC existed on the sample, and that band A and band B corresponded to the two forms. The alkaline treatment was conducted by immersing the

substrate into a NaOH solution for about 60 seconds and by blow drying with nitrogen gas. The alkaline solution was prepared using 5-mM NaOH aqueous solution and ethanol in a volume ratio of 1:200. The SFG spectra of the monolayer measured before and after the alkaline treatment with 480-nm probe are shown in Figure 3.4. Band B disappeared and band A increased in intensity after the treatment. This result suggests that two different chemical species existed on the sample, and that by the alkaline treatment, the species corresponding to band B was converted to the other species corresponding to band A. In other words, the change in the SFG spectrum with the treatment resulted from shifting of the chemical equilibrium of different forms of FITC on the substrate. Thus, band A should correspond to a deprotonated species and band B to a protonated one.

The FITC molecule has three sites where a proton can be attached or detached, and takes four forms (cation, neutral, anion, and dianion, see Figure 3.1) depending on the pH in aqueous solutions. In estimating the observed, deprotonated and protonated forms on platinum, we supposed that the FITC molecule on metal, as well as in aqueous solution, can take the form of cation, neutral, anion and dianion, and compared the SFG excitation profiles with the electronic absorption spectra of fluorescein in the solution phase.

Sjöback and co-workers [9] measured the pH dependence of absorption and fluorescence spectra of fluorescein aqueous solutions and, by deconvolution of the observed spectra, obtained the absorption spectra of cation, neutral, anion, and dianion forms in the 250-550 nm wavelength region. Mchedlov-Petrosyan et al. [10] reported that the electronic absorption spectra of the four protolytic forms of FITC in aqueous solutions for the spectral region from 435 to 515 nm. According to the report [10], the absorption spectra of each protolytic form of FITC in aqueous solution were, without being affected by the isothiocyanate (-NCS) group of FITC, almost identical to those of corresponding forms of fluorescein in aqueous solutions. Since the reported wavelength region of FITC is limited, the spectra of fluorescein will be used for comparison with the DR-SFG excitation profiles in the following section.

The DR-SFG excitation profiles for bands A and B were compared with the electronic absorption spectra of the four protolytic forms of fluorescein in aqueous solution [9] as shown in Figure 3.3. The comparison revealed that the profiles of bands A and B (Fig. 3.3 (a), (b)) resemble the electronic absorption spectra of anion and neutral forms of fluorescein in aqueous solution, respectively. The absorption spectrum of the neutral form and the excitation profile of band B show their peaks at a shorter wavelength, and have narrower bandwidths than the absorption spectrum of the anionic form and the excitation profile of band A. Based on the similarity, we assigned band A and band B of vibrational DR-SFG spectra to anion and neutral forms on platinum, respectively.

The DR-SFG excitation profile of the 1643-cm^{-1} band after the alkaline treatment was also measured with six probe wavelengths (431, 449, 480, 537, 559, and 582 nm) and found to have the same shape as the profile of band A before the alkaline treatment. The right side of Figure 3.2, R1-R6, shows the SFG spectra of the FITC monolayer on platinum after rinsing with the alkaline solution. Only band A was identified on the six vibrational SFG spectra. The two DR-SFG excitation profiles of band A before and after the alkaline treatment were almost identical (Figure 3.3, (a) and (a')) though the amplitude was increased for the spectrum after the treatment. This increase may be due to the conversion of the neutral species to the anions species. This observation confirms that band A before and after the treatment was caused by the same chemical species.

3.4 Vibrational assignments of the vibrational SFG bands

Vibrational assignments of bands A and B were made with the aid of quantum chemical calculations. Normal coordinate calculations for anion and neutral species as isolated molecules were carried out by the B3LYP method with the basis set 6-31G(d) using the Gaussian 03 [11] program package. The harmonic wavenumbers, the IR intensities, the Raman activities, and pre-resonance Raman activities with a 500-nm Raman probe were calculated on an energy-optimized geometry of each model molecule. The IR intensity and pre-resonance Raman activity are proportional to absorption coefficient and total Raman scattering cross-section of randomly orientated molecules, respectively. The harmonic wavenumbers scaled by 0.9613 [12] will be used in the following discussion because DFT calculations typically predict larger harmonic vibrational wavenumbers than the ones observed experimentally. The results of the calculations are summarized in Table 3.1 and 3.2 for the vibrational modes whose scaled harmonic wavenumbers was in the range of 1550 to 1800 cm^{-1} .

The vibrational resonant term of DR-SFG susceptibility of a vibrational band can be calculated by averaging the tensor product of the IR transition dipole and anti-Stokes Raman tensor of the band over all the orientations of FITC molecules on the substrate. However, we do not know the orientational distribution for the sample at the present time, and therefore used, in the following discussion, the product of the calculated IR intensity and Raman activity of a vibrational mode as a criterion to judge how strong the SFG signal due to the mode is; we assumed that a vibrational mode with a larger product is more likely to be observed in DR-SFG spectra. The anti-Stokes resonance Raman activity was also approximated by a pre-resonance Raman activity with a 500-nm Raman probe.

Band A (1643 cm^{-1} , the anionic form) and band B (1610 cm^{-1} , the neutral form) in the vibrational SFG spectra of the FITC monolayers should be assigned to vibrational modes that contain large contributions from xanthene ring motions because the intensities of both bands were enhanced by electronic resonance in the visible region as seen in their

DR-SFG excitation profiles (Figure 3.3). For the isolated anion, there were four calculated vibrational normal modes that were assignable to xanthene ring stretches in the wavenumber range above 1550 cm^{-1} . The 1602-cm^{-1} calculated mode had the largest product of the IR intensity and the pre-resonance Raman activity. The 1602-cm^{-1} mode is shown in Figure 3.5a. There were two calculated modes whose wavenumbers (1617 , 1637 cm^{-1}) were closer to the observed wavenumber of band A, 1643 cm^{-1} . However, the product of the two modes was much weaker; the products of the 1617-cm^{-1} mode and the 1637-cm^{-1} mode were twelve times and two times smaller than that of the 1602-cm^{-1} mode, respectively. Therefore, we assigned band A to the 1602-cm^{-1} mode of the isolated anion. For the isolated neutral molecule, five xanthene ring stretch modes were calculated in the wavenumber range above 1550 cm^{-1} . Among them, a vibrational mode whose wavenumber was 1604 cm^{-1} had the largest product. The 1653-cm^{-1} mode had the second largest product among the five modes and its product is four times smaller than that of the 1604-cm^{-1} mode. The 1604-cm^{-1} mode was assigned to band B at 1610 cm^{-1} . It is noted that the 1604-cm^{-1} mode of the neutral species is quite similar to the 1602-cm^{-1} mode of the anion species except that the former does not include the stretch of the carbonyl group in the xanthene group.

3.5 Fluorescence excitation spectra of FITC monolayers on platinum

The assignments of surface species were also examined by fluorescence excitation spectra of the monolayers. The fluorescence of the FITC monolayers on platinum was weak but measurable; it was typically more than 100 times weaker than the fluorescence of FITC monolayers on silica prepared by spin-coating. The weakness is probably due to the quenching of fluorescence by electron transfer from molecules to the platinum.

Figure 3.6 shows the fluorescence emission and excitation spectra of the FITC monolayer on platinum before and after the alkaline treatment. The treatment did not affect the shapes of either of the spectra. The shape of the fluorescence excitation spectra was similar to that of absorption spectrum of fluorescein anion in aqueous solutions (Fig. 3.3), though the band in the excitation spectra was red-shifted and broadened compared with the absorption spectrum in aqueous solutions. This observation suggests that the anion form of FITC existed on platinum but its electronic structure was only slightly changed from that of the same protolytic form in aqueous solutions, probably due to the difference between the environments of the molecules.

That the neutral form of FITC was not identified on the fluorescence excitation spectrum of the monolayer before the alkaline treatment may have been due to the fact that the fluorescence quantum yield of the neutral form was negligible. It was reported that, in aqueous solution, the neutral form has no significant fluorescence, while the anion form has a rather large fluorescence quantum yield of 0.37 [9].

The dianion form of fluorescein also has a very large fluorescence quantum yield of 0.93 in aqueous solutions [9]. The fluorescence of dianion of FITC would have been observed if a substantial amount of dianion molecules of FITC had existed on the substrate. However, it was not seen in the fluorescence excitation spectra of the sample. The finding suggests that the dianion form was absent before the treatment, and that the anion and neutral forms were not converted to the dianion form by the treatment.

The DR-SFG excitation profile of band A and the fluorescence excitation spectra of FITC on platinum agreed very well. (See Figure 3.6) The assignment of band A as anionic species of FITC from the SFG measurement is consistent with the result from the fluorescence excitation spectra. It is noted that DR-SFG spectroscopy provides the information on what protolytic forms of FITC are present on the substrate, even if they are not detected by electronic absorption or fluorescence measurements.

3.6 Summary

We performed DR-SFG spectroscopy of FITC monolayers on platinum substrates. The vibrational SFG spectra of the monolayers consisted of two vibrational bands at 1643 and 1610 cm^{-1} , and the DR-SFG excitation profiles of these vibrational bands were different from each other. To elucidate the origin of the different DR-SFG excitation spectral shapes, an FITC monolayer on platinum was treated with alkaline solution. Based on the response of vibrational SFG and DR-SFG excitation spectra to the treatment, we clarified that there were two chemical species of FITC on platinum and assigned one to the anion form and the other to the neutral form. To verify this, fluorescence excitation spectra were also measured, and they supported the assignments of the chemical species. The study demonstrated that interface selective DR-SFG provided an effective technique to identify chemical species at interfaces where various chemical species co-exist, since DR-SFG excitation spectra of different chemical species offer valuable information on their electronic structure.

Appendix A. Fresnel factors

The effective nonlinear susceptibility, χ_{eff} , consists of orientationally-averaged molecular hyperpolarizability and the Fresnel coefficients; the former depends on the orientational distribution of adsorbed molecules, and the latter mainly consists of the refractive index of the substrate. The Fresnel factors can dominate the spectral shape of DR-SFG excitation profiles because they depend on the probe wavelengths. We examined the influence of the Fresnel factors on the excitation profiles, and found that they do not vary much and have little impact on the shapes of the profiles.

The effective second-order nonlinear susceptibility of an azimuthally isotropic sample for p-polarized visible and IR probes is given by [13]

$$\begin{aligned}\chi_{\text{eff}} = & -L_{xx}(\omega_{\text{SFG}})L_{xx}(\omega_{\text{VIS}})L_{zz}(\omega_{\text{IR}})\cos\beta_{\text{SFG}}\cos\beta_{\text{VIS}}\sin\beta_{\text{IR}}\chi_{xxz} \\ & -L_{xx}(\omega_{\text{SFG}})L_{zz}(\omega_{\text{VIS}})L_{xx}(\omega_{\text{IR}})\cos\beta_{\text{SFG}}\sin\beta_{\text{VIS}}\cos\beta_{\text{IR}}\chi_{xxz} \\ & +L_{zz}(\omega_{\text{SFG}})L_{xx}(\omega_{\text{VIS}})L_{xx}(\omega_{\text{IR}})\sin\beta_{\text{SFG}}\cos\beta_{\text{VIS}}\cos\beta_{\text{IR}}\chi_{xxz} \\ & +L_{zz}(\omega_{\text{SFG}})L_{zz}(\omega_{\text{VIS}})L_{zz}(\omega_{\text{IR}})\sin\beta_{\text{SFG}}\sin\beta_{\text{VIS}}\sin\beta_{\text{IR}}\chi_{zzz}\end{aligned}\quad (3-2)$$

where $L_{xx}(\omega)$ and $L_{zz}(\omega)$ are the Fresnel factors at frequency ω ; β_{SFG} , $\beta_{\text{VIS}} (= 70^\circ)$, and $\beta_{\text{IR}} (= 50^\circ)$ are the angles between the surface normal and the SFG, VIS probe, and IR probe beams, respectively; and χ_{ijk} ($i, j, k = x$ or z) are the non-vanishing elements of the second-order nonlinear susceptibility. The z direction was chosen to be parallel to the surface normal, and xz -plane the incidence plane of the probe beams. $L_{xx}(\omega_{\text{IR}})$ is much smaller than $L_{zz}(\omega_{\text{IR}})$ because the sample was on metal, so Eq. (3-2) is reduced to the form as follows:

$$\begin{aligned}\chi_{\text{eff}} = & -L_{xx}(\omega_{\text{SFG}})L_{xx}(\omega_{\text{VIS}})L_{zz}(\omega_{\text{IR}})\cos\beta_{\text{SFG}}\cos\beta_{\text{VIS}}\sin\beta_{\text{IR}}\chi_{xxz} \\ & +L_{zz}(\omega_{\text{SFG}})L_{zz}(\omega_{\text{VIS}})L_{zz}(\omega_{\text{IR}})\sin\beta_{\text{SFG}}\sin\beta_{\text{VIS}}\sin\beta_{\text{IR}}\chi_{zzz}\end{aligned}\quad (3-3)$$

Two factors in Eq. (3-3), $F_{xxz} \equiv |L_{xx}(\omega_{\text{SFG}})L_{xx}(\omega_{\text{VIS}})\cos\beta_{\text{SFG}}\cos\beta_{\text{VIS}}|$ and $F_{zzz} \equiv |L_{zz}(\omega_{\text{SFG}})L_{zz}(\omega_{\text{VIS}})\sin\beta_{\text{SFG}}\sin\beta_{\text{VIS}}|$ were calculated and plotted against the SFG wavelength in Figure 3.7. (The Fresnel factors were calculated using the Eqns in Ref. 13 and the

refractive index of interfacial layer was assumed to be 1.) The Fresnel factors were calculated with the values of complex refractive indices of platinum from the literature [14]. F_{zzz} is much larger than F_{xxz} , and hence the second term of the right-hand side of Eq. (3-3) may control the effective susceptibility, and F_{zzz} monotonically increases with the SFG wavelength, and its variation for the 405–530 nm wavelength regions is about 20%. On the basis of the small variation, we concluded that the Fresnel factors do not have much effect on the spectral shape of the DR-SFG excitation profile.

Appendix B. Improvement in measuring of vibrational SFG spectra and DR-SFG excitation profiles of the FITC monolayer on platinum

Measuring the vibrational spectra with several visible probe wavelengths to obtain DR-SFG electronic excitation profiles is time-consuming. For example, it took two or three days to measure vibrational SFG spectra of the FITC monolayer on platinum with six visible probe wavelengths shown in Figure 3.2. To make the measuring process more efficient, I modified our multiplex SFG spectrometer. As the result of the modification, parameters of the spectrometer have been controllable by a PC, and the time required to measure DR-SFG excitation profile has become significantly shorter.

A program implemented on Igor Pro (WaveMetrics, Inc.) software platform was used to measure a series of vibrational SFG spectra with different visible probe wavelengths. It controls the wavelength, pulse energy, and optical delay of the visible probe as well as the center wavelength of the polychromator. When the wavelength of the visible probe is changed, the temporal and spatial positions of the visible probe are also changed a little. The optical delay and the position of the focusing lens are controlled so that these changes are compensated. At every visible probe wavelength, SFG spectra of the sample and a reference (e.g. a silver mirror, ER.2, Newport Inc.) were alternately recorded several times, so that fluctuation of the visible and IR probes may be partly canceled. The schematic diagram for the measurement is shown in Figure 3.8. The procedure of the measurement of the vibrational SFG spectrum is as follows:

1. set the silver mirror at the sample position by changing the position of the sample stages, and set up the OD value of ND filter appropriate for measurement of the mirror by rotating the ND filter wheel.
2. measure the SFG spectrum of the silver mirror.
3. set the FITC monolayer at the sample position by changing the position of the sample stages, and set up the OD value of ND filter appropriate for measurement of the

monolayer by rotating the ND filter wheel.

4. measure the SFG spectrum of the FITC monolayer on platinum.
5. repeat the procedure 1.
6. measure the SFG spectrum of the silver mirror again.
7. repeat the procedure 3.
8. block the IR probe.
9. measure the contribution of the stray light by the visible probe for the spectrum of the monolayer.
10. repeat the procedure 1.
11. measure the contribution of the stray light by the visible probe for the spectrum of the silver mirror.
12. change the wavelength of the visible probe

The intensity of each SFG spectrum of the FITC sample is calibrated by dividing the spectrum by the one of a silver mirror measured with each probe wavelength. The SFG susceptibility of the silver mirror is expected to be independent of the visible probe wavelength.

Figure 3.9 shows the vibrational SFG spectra of the FITC monolayer on platinum before the alkaline treatment with 31 visible probes (430-580 nm) with ppp polarization combination. The fitting results with eq. (3-1), the red lines, were also shown in the figure. The vibrational spectra in Figure 3.9 (a) and (b) were obtained with signal outputs and second harmonics of idler outputs of the ps OPA for the visible probe, respectively. Although the number of visible probe wavelengths (31) used for obtaining the vibrational spectra was much larger than that (6) for Figure 3.2, it took only 2 days for the measurement.

Figure 3.10 shows the SFG excitation profiles measured with 31 visible probes for the vibrational bands A and B. It was found that the excitation profiles measured with 31 visible probes are almost similar to those measured with 6 visible probes for both bands.

The similarity indicates that SFG excitation spectra with the improved method are as reliable as those with the conventional method.

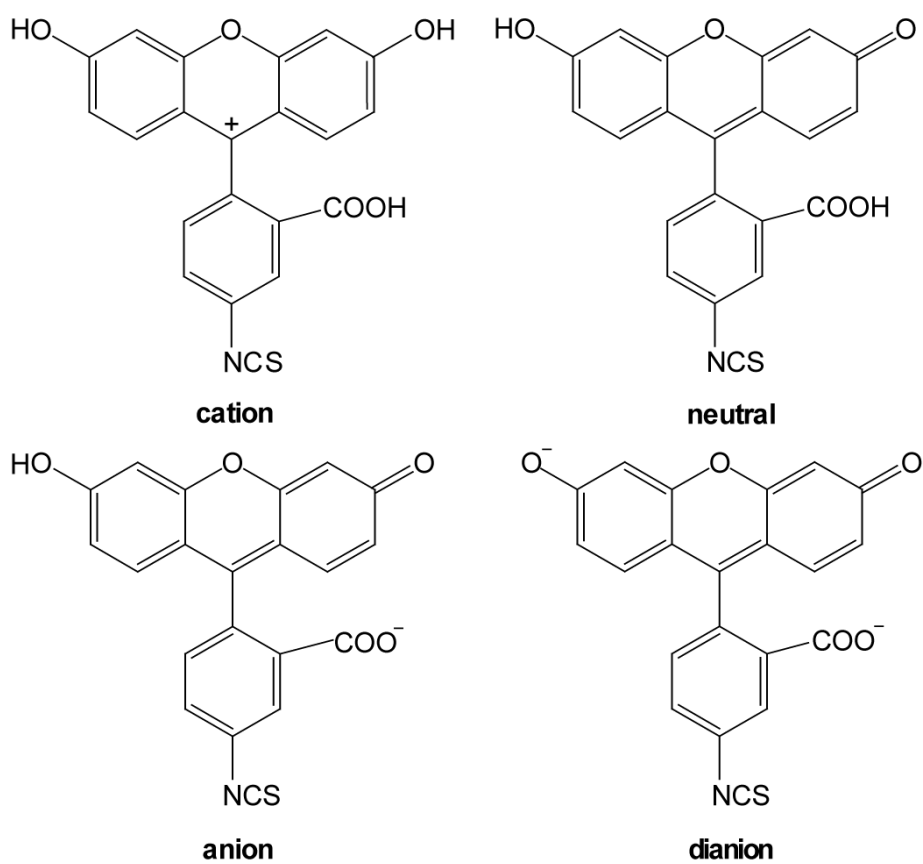


Figure 3.1 Four protolytic forms of fluorescein isothiocyanate isomer-I

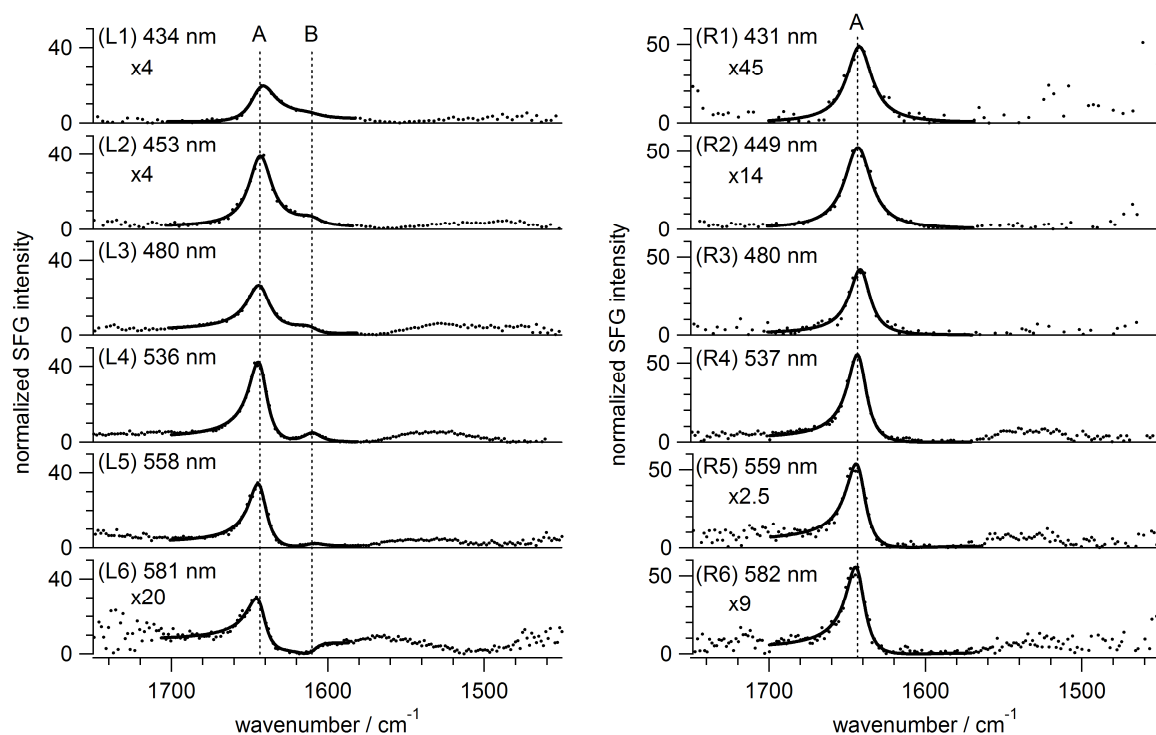


Figure 3.2 Vibrational SFG spectra of FITC monolayers on platinum substrates. Left (L1-L6): spectra before the alkaline treatment. Right (R1-R6): spectra after the alkaline treatment. Visible probe wavelengths of each spectra are indicated in the figure. The SFG intensities of the spectra of (L1), (L2), (L6), (R1), (R2), (R5), and (R6) are scaled as indicated. The intensities of the SFG spectra of FITC on platinum were normalized against that of Y-cut quartz.

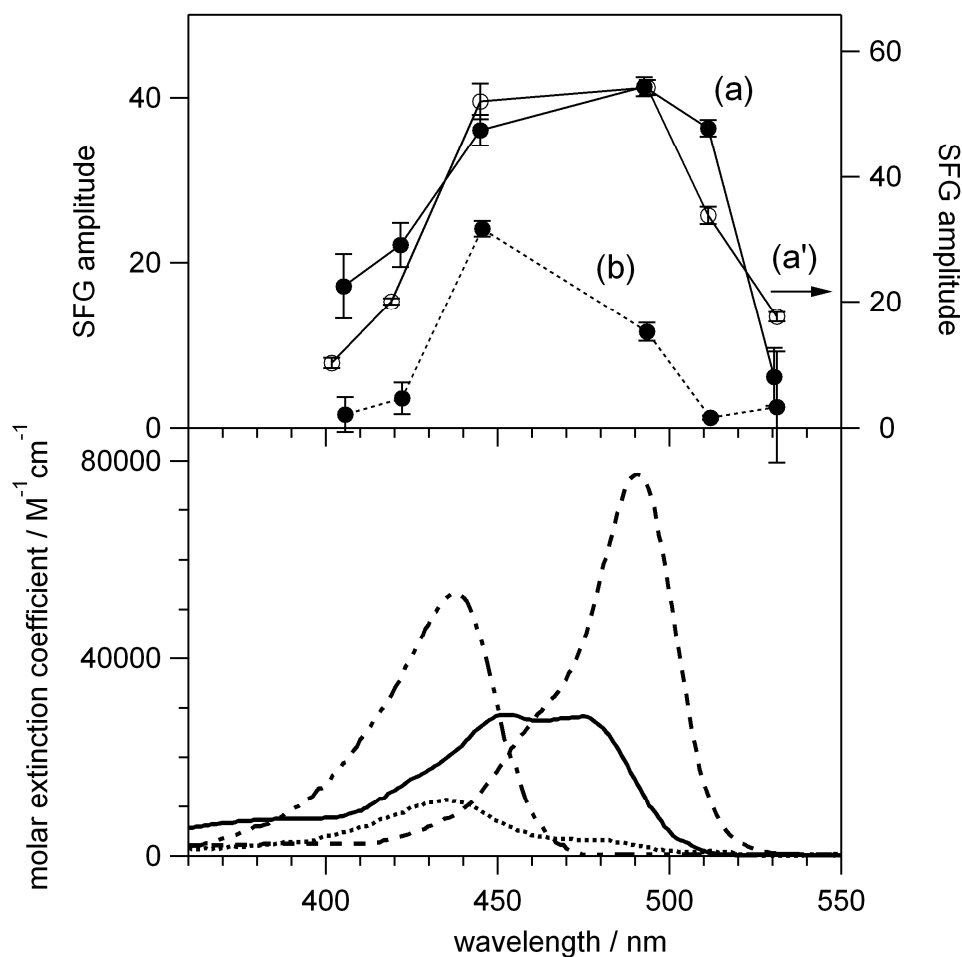


Figure 3.3 Upper panel: SFG excitation profiles of FITC monolayers on platinum. (a) The amplitude of band A (1643 cm⁻¹) before the alkaline treatment, (a') the amplitude of band A after the alkaline treatment, and (b) the amplitude of band B (1610 cm⁻¹) before the alkaline treatment. Lower panel: Electronic absorption spectra of the four protolytic forms of fluorescein (cation, ····; neutral species, ···; anion, —; dianion, ---) in aqueous solutions. Absorption spectra were reproduced from Figure 1 of Ref. 9.

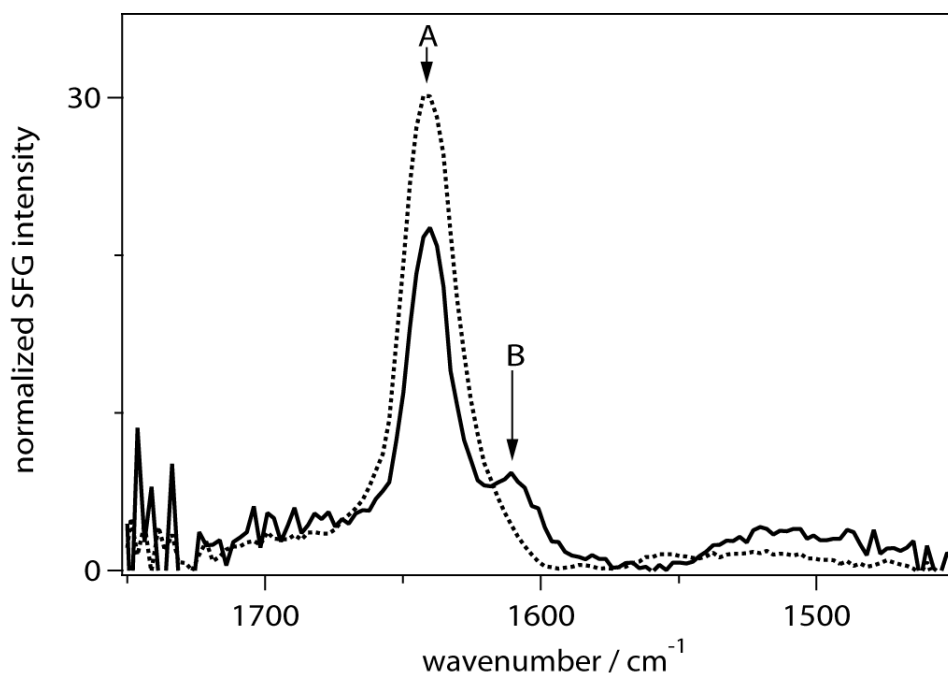
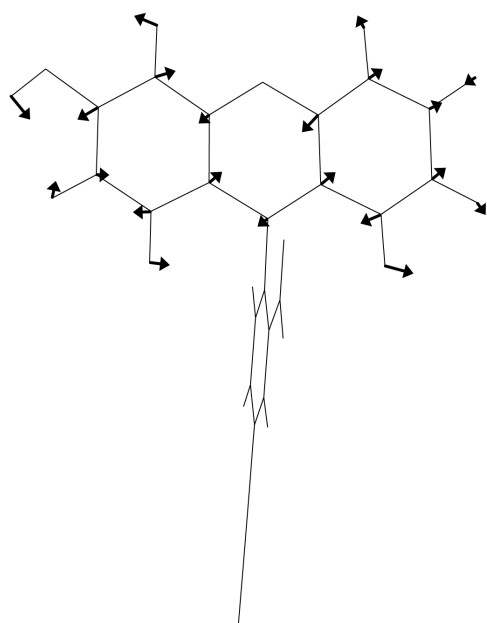


Figure 3.4 Vibrational SFG spectra of an FITC monolayer on platinum before and after the alkaline treatment. Solid line: before the treatment, dotted line: after the treatment. Visible probe wavelength: 480 nm. The intensities of the SFG spectra were normalized against that of Y-cut quartz.

(a) anion

1602 cm^{-1}



(b) neutral

1604 cm^{-1}

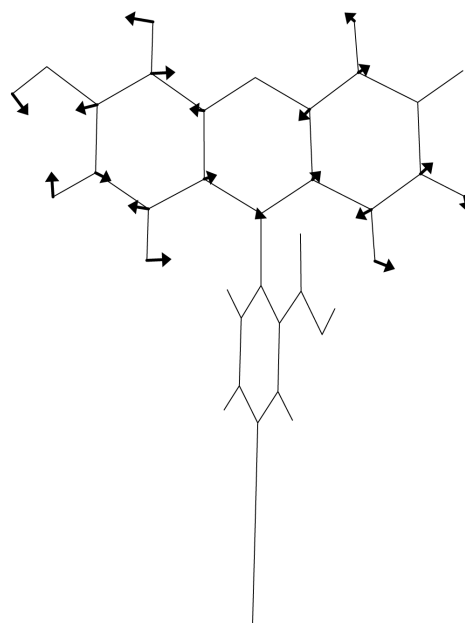


Figure 3.5 Vibrational normal modes of anion and neutral species of FITC calculated by the B3LYP method with the basis set 6-31G(d). (a) the mode of anion species assigned to band A, (b) the mode of neutral species assigned to band B.

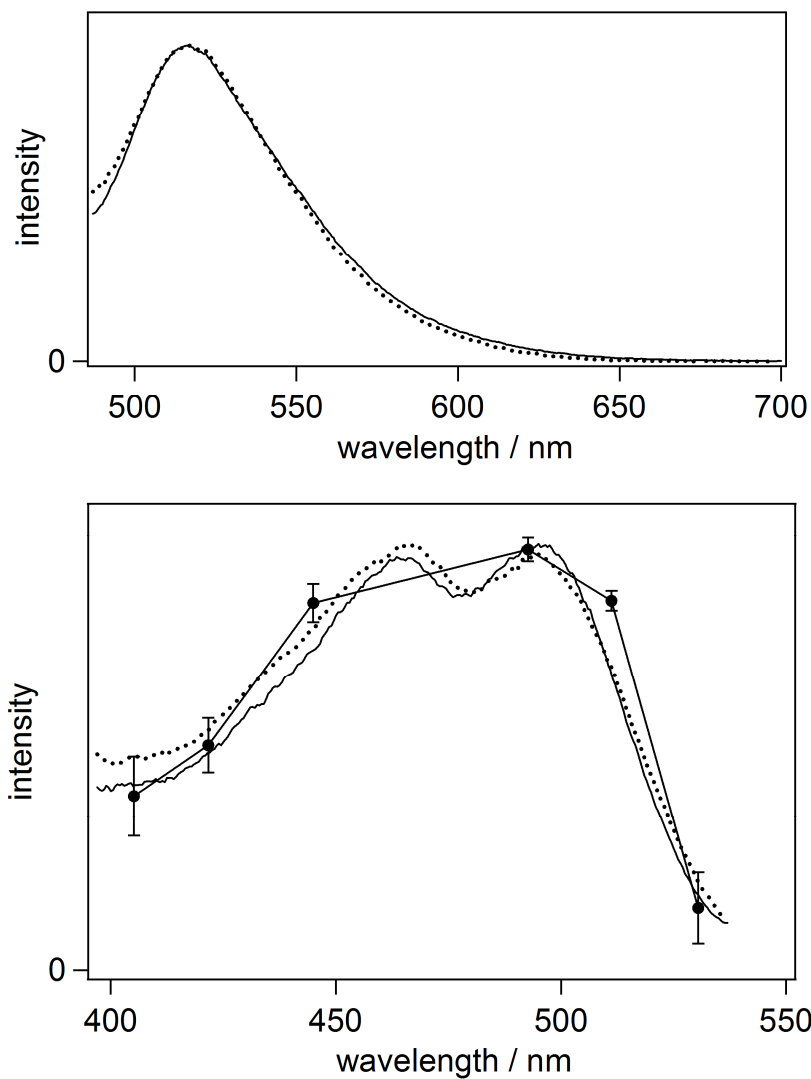


Figure 3.6 Upper panel: fluorescence spectra of the FITC monolayer on platinum before and after the alkaline treatment (before the treatment, dotted line; after the treatment, solid line). Excitation wavelength, 430 nm; slit width, 10 nm. Lower panel: fluorescence excitation spectra of the FITC monolayer on platinum before and after the alkaline treatment and DR-SFG excitation profiles of band A before the treatment. Dotted line: fluorescence excitation spectra before the treatment, solid line: fluorescence excitation spectra after the treatment, and filled circle: SFG excitation profile of band A before the treatment. Fluorescence intensity was monitored at 565 nm, and the slit width of the monochromator for the excitation light was 10 nm.

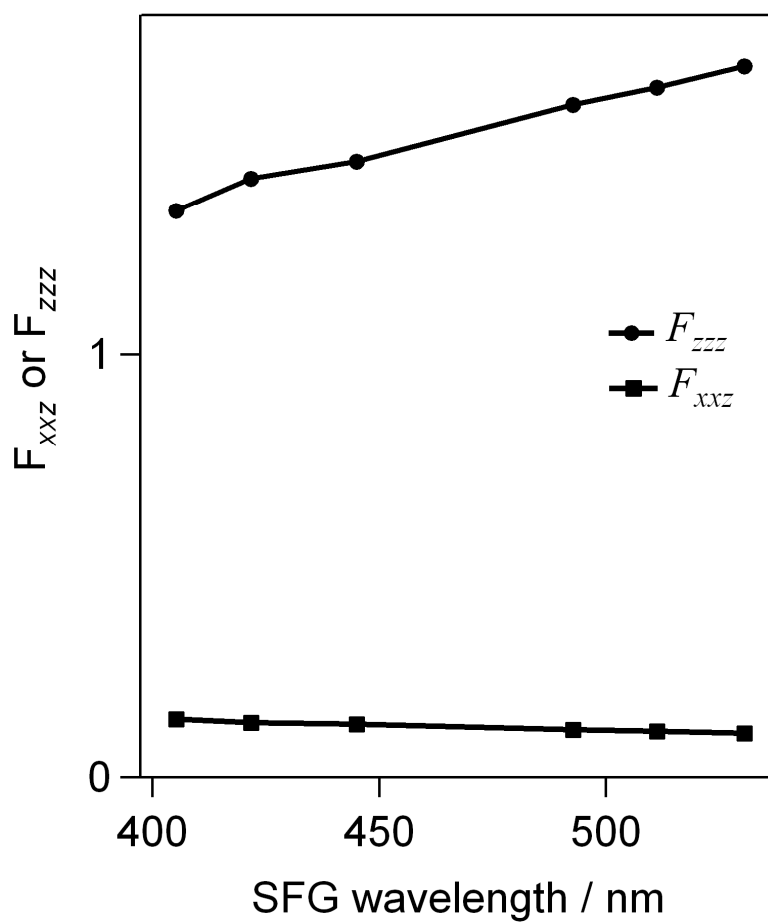


Figure 3.7 F_{zzz} and F_{xxz} versus SFG wavelength. F_{zzz} : filled circle, F_{xxz} : filled square.

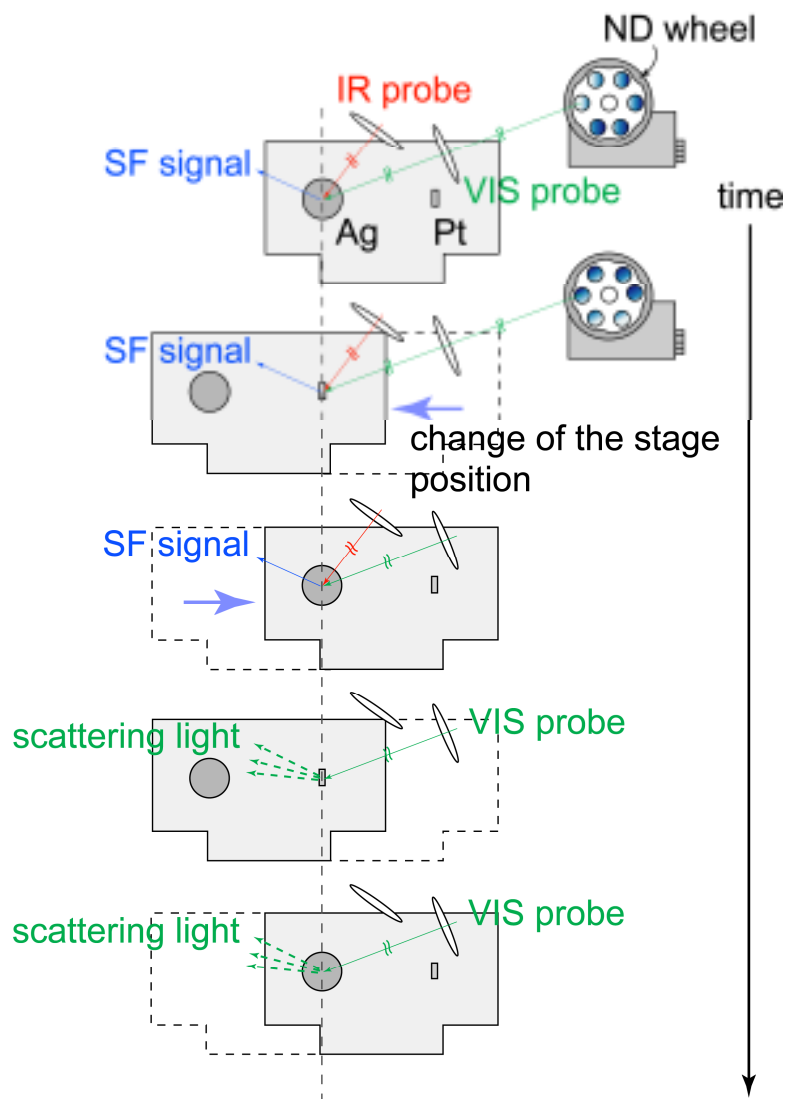


Figure 3.8 The measurement scheme of SFG spectra with an improved PC-controlled SFG spectroemter.

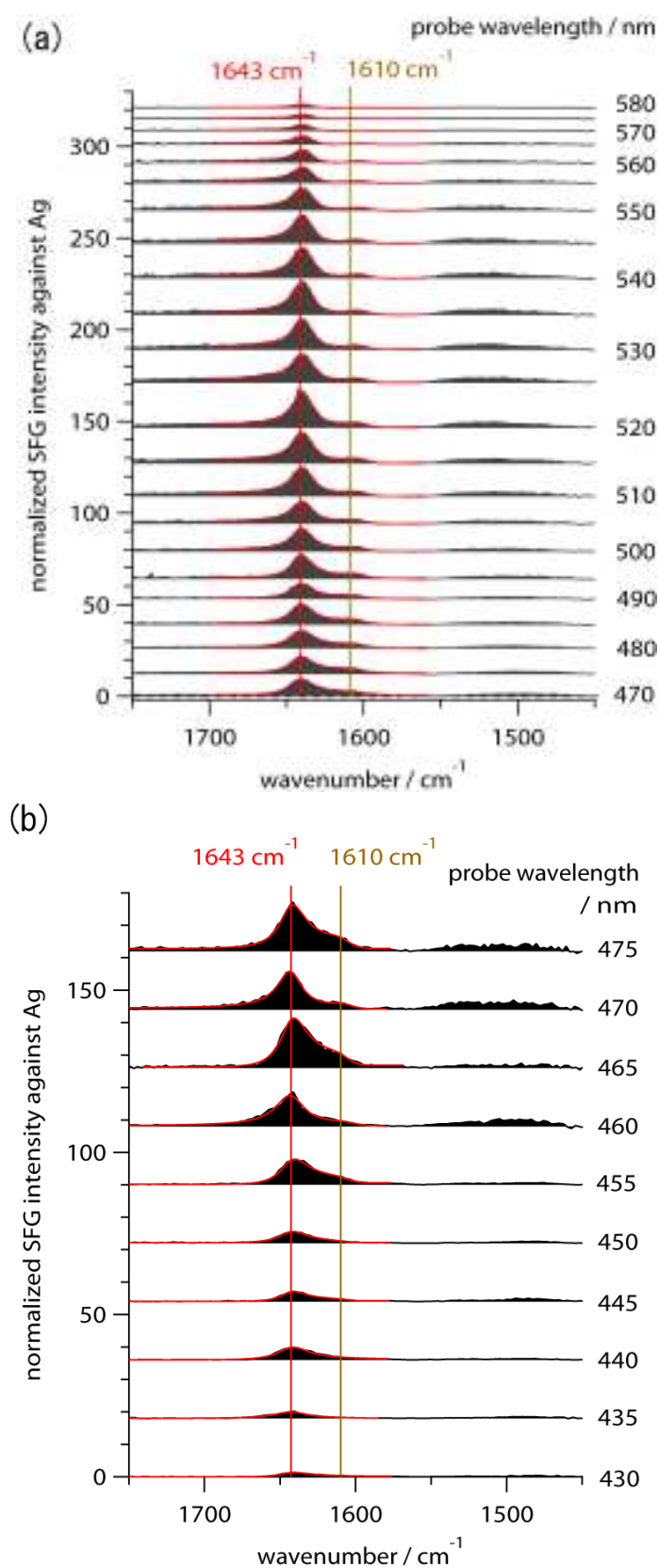


Figure 3.9 Vibrational SFG spectra of the FITC monolayer on a platinum substrate. (a) SFG spectra with signal outputs of OPA. (b) SFG spectra with second harmonics of idler outputs of ps OPA. The intensities of the SFG spectra of FITC on platinum were normalized against that of a silver mirror.

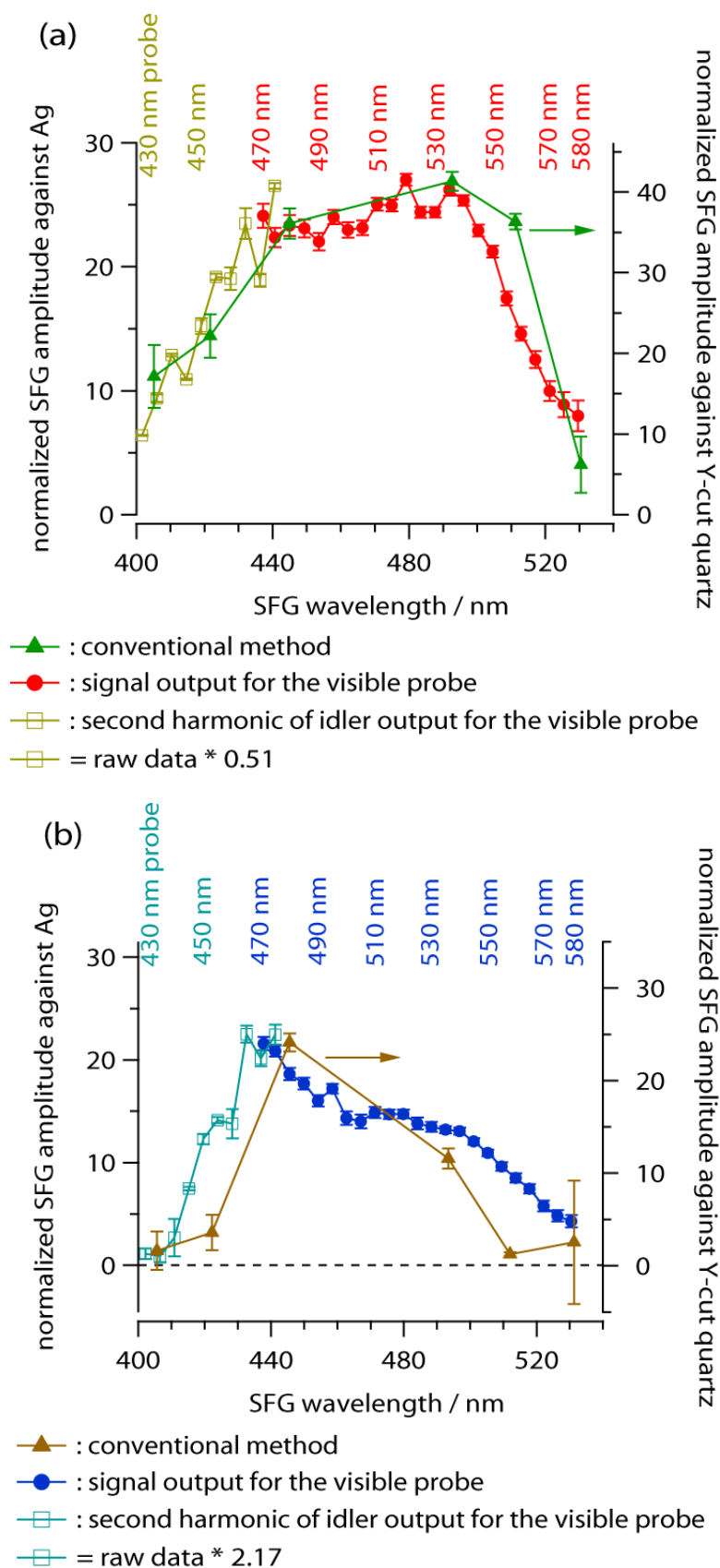


Figure 3.10 SFG excitation profiles of the FITC monolayer on platinum. (a) the amplitude of band A (1643 cm^{-1}) before the alkaline treatment. (b) the amplitude of band B (1610 cm^{-1}) before the alkaline treatment.

| mode number ^a | scaled harmonic wavenumber ^b | IR intensity | Raman Activity | pre-resonance Raman activity | the products of IR intensity and pre-resonance Raman activity | mode description |
|--------------------------|---|--------------|----------------|------------------------------|---|------------------|
| 92 | 1570 | 201 | 208 | 3832 | 770232 | xanthene ring |
| 93 | 1578 | 80 | 1444 | 12094 | 967520 | phenyl ring |
| 94 | 1602 | 306 | 441 | 69880 | 21383280 | xanthene ring |
| 95 | 1617 | 236 | 194 | 7579 | 1788644 | xanthene ring |
| 96 | 1637 | 778 | 352 | 12167 | 9465926 | xanthene ring |
| 97 | 1675 | 437 | 78 | 38238 | 16710006 | -COO |

^a Natural number starting from 1 are assigned to modes in ascending order of harmonic wavenumber.

^b The scale factor: 0.9613.

Scaled harmonic wavenumbers, cm^{-1} ; IR intensities, km mol^{-1} ; preresonance Raman activities with 500 nm probe, $\text{\AA}^4 \text{amu}^{-1}$; the products of IR intensity and preresonance Raman activity, $\text{km mol}^{-1} \text{\AA}^4 \text{amu}^{-1}$.

Table 3.1 Results of vibrational analysis for the anionic species of FITC at DFT/6-31G(d) in the range 1550–1800 cm^{-1}

| mode number ^a | scaled harmonic wavenumber ^b | IR intensity | Raman Activity | pre-resonance Raman activity | the products of IR intensity and pre-resonance Raman activity | mode description |
|--------------------------|---|--------------|----------------|------------------------------|---|------------------|
| 93 | 1556 | 126 | 15 | 4291 | 540666 | xanthene ring |
| 94 | 1567 | 137 | 76 | 1525 | 208925 | xanthene ring |
| 95 | 1588 | 73 | 1404 | 5703 | 416319 | phenyl ring |
| 96 | 1604 | 450 | 929 | 60087 | 27039150 | xanthene ring |
| 97 | 1635 | 45 | 158 | 20416 | 918720 | xanthene ring |
| 98 | 1653 | 468 | 502 | 14027 | 6564636 | xanthene ring |
| 99 | 1758 | 334 | 41 | 546 | 182364 | -COOH |

^a Natural number starting from 1 are assigned to modes in ascending order of harmonic wavenumber.

^b The scale factor: 0.9613.

Scaled harmonic wavenumbers, cm^{-1} ; IR intensities, km mol^{-1} ; preresonance Raman activities with 500 nm probe, $\text{\AA}^4 \text{amu}^{-1}$; the products of IR intensity and preresonance Raman activity, $\text{km mol}^{-1} \text{\AA}^4 \text{amu}^{-1}$.

Table 3.2 Results of vibrational analysis for the neutral species of FITC at DFT/6-31G(d) in the range 1550–1800 cm^{-1}

References

- [1] C. W. Griffin, T. R. Carski, G. S. Warner, *J. Bacteriol.* **82**, 534-537 (1961).
- [2] L. Kaufman and W. Kaplan, *J. Bacteriol.* **82**, 729-735 (1961).
- [3] J. L. Riggs, R. J. Seiwald, J. H. Burckhalter, C. M. Downs and T. G. Metcalf, *Am. J. Pathol.* **34**, 1081-1097 (1958).
- [4] W. B. Cherry, R. M. Mckinney, V. M. Emmel, J. T. Spillane, G. A. Hebert and B. Pittman, *Stain Technol.* **44**, 179-186 (1969).
- [5] S. C. Chen, H Nakamura and Z. Tamura, *Chem. Pharm. Bull.* **27**, 475-479 (1979).
- [6] Y. R. Shen, *Proc. Natl. Acad. Sci. U.S.A.* **93**, 12104-12111 (1996).
- [7] M. B. Raschke, M. Hayashi, S. H. Lin and Y. R. Shen, *Chem. Phys. Lett.* **359**, 367-372 (2002).
- [8] Y. Caudano, C. Silien, C. Humbert, L. Dreesen, A. A. Mani, A. Peremans and P. A. Thiry, *J. Electron Spectrosc. Relat. Phenom.* **129**, 139-147 (2003).
- [9] R. Sjöback, J. Nygren and M. Kubista, *Spectrochim. Acta, Part A*, **51**, L7-L21 (1995).
- [10] N. O. Mchedlov-Petrosyan, Y. V. Isaenko, N. A. Vodolazkaya and S. T. Goga, *CPS Physchem.* 0309005 (2003).
- [11] M. J. Frisch, G. W. Trucks, H. B. Schlegel, G. E. Scuseria, M. A. Robb, J. R. Cheeseman, Montgomery, Jr., J. A., T. Vreven, K. N. Kudin, J. C. Burant, J. M. Millam, S. S. Iyengar, J. Tomasi, V. Barone, B. Mennucci, M. Cossi, G. Scalmani, N. Rega, G. A. Petersson, H. Nakatsuji, M. Hada, M. Ehara, K. Toyota, R. Fukuda, J. Hasegawa, M. Ishida, T. Nakajima, Y. Honda, O. Kitao, H. Nakai, M. Klene, X. Li, J. E. Knox, H. P. Hratchian, J. B. Cross, V. Bakken, C. Adamo, J. Jaramillo, R. Gomperts, R. E. Stratmann, O. Yazyev, A. J. Austin, R. Cammi, C. Pomelli, J. W. Ochterski, P. Y. Ayala, K. Morokuma, G. A. Voth, P. Salvador, J. J. Dannenberg, V. G. Zakrzewski, S. Dapprich, A. D. Daniels, M. C. Strain, O. Farkas, D. K. Malick, A. D. Rabuck, K. Raghavachari, J. B. Foresman, J. V. Ortiz, Q. Cui, A. G. Baboul, S. Clifford, J. Cioslowski, B. B. Stefanov, G. Liu, A. Liashenko, P. Piskorz, I. Komaromi, R. L. Martin, D. J. Fox, T. Keith, M. A. Al-Laham, C. Y. Peng, A. Nanayakkara,

M. Challacombe, P. M. W. Gill, B. Johnson, W. Chen, M. W. Wong, C. Gonzalez and J. A. Pople *Gaussian 03, Revision D.01*. Gaussian, Wallingford, 2004.

[12] M. W. Wong, Chem. Phys. Lett. **256**, 391-399 (1996).

[13] X. Zhuang, P. B. Miranda, D. Kim and Y. R. Shen, Phys. Rev. B **59**, 12632-12640 (1999).

[14] E. D. Palik (ed). *Handbook of Optical Constants of Solids*, Academic Press: New York (1985).

**Chapter 4. Doubly Resonant Sum-Frequency
Generation Spectroscopy on Thin Films of N,
N'-bis(octyl)perylene-3,4,9,10-tetracarboxylic
diimide on SiO₂ Substrates**

4.1 Introduction

In this study, I applied DR-SFG spectroscopy to thin-layer samples of organic semiconductor deposited on silica substrates. Organic semiconductors are used for molecular devices such as organic light emitting diodes (OLEDs) and organic field effect transistors (OFETs). They have been attracting much attention as electronic devices that will replace widely used silicon-based electronic devices. Most of such molecular devices have a single- or multi-thin layer structures and their performances are expected to depend greatly on molecular structures at interfaces. Therefore it is very interesting to probe interfaces of organic semiconductor thin layers by using vibrational SFG that are forbidden in centrosymmetric bulk layer under the electronic-dipole approximation. The samples that I have applied vibrational SFG to are N,N'-bis(octyl)perylene-3,4,9,10-tetracarboxylic diimide (PTCDI-C₈, Figure 1.2) thin layers on silica substrates. PTCDI-C₈ is an organic semiconductor material used in OFETs. The bulk layer of PTCDI-C₈ is known to form the center of inversion and hence is SFG inactive. If an SFG signal is obtained from a thin film of PTCDI-C₈, the primary source of the signal should be two interfaces, i.e. the air-semiconductor and semiconductor-silica interfaces. To estimate the extent to which each interface contributes to the signal, we have examined the thickness dependence of SFG signal. The contributions to the observed DR-SFG signal from both interfaces are expected to be greatly modulated with the film thickness. This is because the semiconductor layer absorbs the visible probe and SFG photons under electronic resonance conditions. The quantitative analysis of the thickness dependence has been performed using a model for the effective SFG susceptibility of a thin film. The model is formulated based on the Fresnel coefficients. The analysis was extended to an advanced model that includes a contribution from the electric quadrupole of the bulk layer. The quadrupole contribution is beyond the electric-dipole approximation. The contribution may not be ignored a priori though it is a high-order contribution. As a result, I could not exclude the possibility that some of the observed SFG signals from the PTCDI-C₈ thin layer samples

were contributed by the bulk, but I concluded that the bulk contribution, if exist, did not overwhelm contributions from interfaces.

4.2 Experimental

An amplified Ti:Sapphire laser (Legend Elite, Coherent), instead of the existing laser system (TITAN II, Quantronix), was used to generate the fundamental output (800 nm, 110 fs, 3.2 mJ, 1 kHz). The output was converted to IR and visible probe pulses.

A silica wafer was purchased from Pier Optics Co. Ltd. The substrate was immersed in a 1:1 mixture of 95wt% H₂SO₄ and H₂O₂ (30% water solution) for 10 min. Then they were washed with purified water and dried. The cleaned substrate was kept in a PFA container including neat hexamethyldisilazane (HMDS) at room temperature for about 12 h. After the treatment with HMDS, the substrate was rinsed with dehydrated methanol to remove redundant HMDS. The PTCDI-C₈ was purchased from Sigma-Aldrich Co. Ltd. and purified by vacuum sublimation. Films of PTCDI-C₈ with different thicknesses were formed on the substrates at a rate of about 0.01 nm/second and at room temperature below 10⁻⁴ Pa by vacuum vapor deposition.

4.3 Theory

The SFG intensity I_{SFG} is proportional to the square of the effective second-order nonlinear susceptibility $\chi_{\text{eff}}^{(2)}$ as follows

$$I_{\text{SFG}} \propto \left| \chi_{\text{eff}}^{(2)} \right|^2. \quad (4-1)$$

Here, $\chi_{\text{eff}}^{(2)}$ takes the form of

$$\chi_{\text{eff}}^{(2)} = [\hat{\mathbf{e}}(\omega_{\text{SF}}) \cdot \mathbf{L}(\omega_{\text{SF}})] \cdot \chi^{(2)} : [\hat{\mathbf{e}}(\omega_{\text{Vis}}) \cdot \mathbf{L}(\omega_{\text{Vis}})] [\hat{\mathbf{e}}(\omega_{\text{IR}}) \cdot \mathbf{L}(\omega_{\text{IR}})] \quad (4-2)$$

with $\hat{\mathbf{e}}(\omega)$ being the unit polarization vector and $\mathbf{L}(\omega)$ the Fresnel factor at frequency ω [1].

The tensor components of $\chi_{\text{eff}}^{(2)}$ can be expressed in terms of Cartesian components of the SFG susceptibility $\chi^{(2)}$ and Fresnel factors [1]. Assuming that an interface is azimuthally isotropic, the ssp SFG signal is then solely contributed by the yyz Cartesian component of the orientationally averaged molecular hyperpolarizability, $\chi_{yyz} = \langle \alpha_{yyz} \rangle$. Henceforth χ_{yyz} is called a Cartesian susceptibility for simplicity. Here, it is assumed that the surface normal of the sample surface is z -axis and the incidence plane is xz -plane. The frequency dependence of $\chi_{\text{eff}}^{(2)}$ can be expressed by the sum of a constant and Lorentz functions [2]. As a result, we obtain the following formulation for $\chi_{\text{eff}}^{(2)}$:

$$\chi_{\text{eff,ssp}}^{(2)} = L_{yy}(\omega_{\text{SF}}) L_{yy}(\omega_{\text{Vis}}) L_{zz}(\omega_{\text{IR}}) \sin \beta_{\text{IR}} \chi_{yyz} = \chi_{\text{NR}} + \sum_q \frac{A_q e^{i\theta_q}}{\omega_{\text{IR}} - \omega_q + i\Gamma_q} \quad (4-3)$$

where $L_{yy}(\omega)$ and $L_{zz}(\omega)$ are Fresnel factors for the light of frequency ω ; β_{IR} is the angle between the surface normal and IR probe beam; χ_{NR} denotes the nonresonant $\chi^{(2)}$; and A_q , ω_q , Γ_q , and ϕ_q refer to the amplitude, resonant frequency, damping coefficient and phase of the q th resonant vibrational mode, respectively. The fitting equation for an SFG spectrum is described as:

$$I_{\text{SFG}} = c_1 \left| \chi_{\text{NR}} + \sum_q \frac{A_q e^{i\theta_q}}{\omega_{\text{IR}} - \omega_q + i\Gamma_q} \right|^2 \quad (4-4)$$

The quantity c_1 is the proportional factor and assumed to be 1 in this paper.

Under the electric-dipole approximation, the possible sources of an SFG signal

from the PTCDI-C₈ film on a SiO₂ substrate are the air/PTCDI-C₈ and PTCDI-C₈/SiO₂ interfaces. Because the SFG field is coherent, the signal radiation fields from both interfaces should interfere with each other to give the detected SFG signal. In this case, $\chi_{\text{eff,ssp}}^{(2)}$ can be given by

$$\chi_{\text{eff,ssp}}^{(2)} = \chi_{\text{NR}} + F_{\text{yyz}}^{\text{surface}} \chi_{\text{yyz}}^{\text{surface}} + F_{\text{yyz}}^{\text{interface}} \chi_{\text{yyz}}^{\text{interface}} \quad (4-5)$$

with

$$F_{\text{yyz}}^{\text{surface}} = L_{\text{yy}}^{\text{surface}}(\omega_{\text{SF}}) L_{\text{yy}}^{\text{surface}}(\omega_{\text{Vis}}) L_{\text{zz}}^{\text{surface}}(\omega_{\text{IR}}) \sin \beta_{\text{IR}} \quad (4-6)$$

$$F_{\text{yyz}}^{\text{interface}} = L_{\text{yy}}^{\text{interface}}(\omega_{\text{SF}}) L_{\text{yy}}^{\text{interface}}(\omega_{\text{Vis}}) L_{\text{zz}}^{\text{interface}}(\omega_{\text{IR}}) \sin \beta_{\text{IR}} \quad (4-7)$$

where $\chi_{\text{yyz}}^{\text{surface}}$ and $\chi_{\text{yyz}}^{\text{interface}}$ are the Cartesian susceptibility of the air/PTCDI-C₈ surface and the PTCDI-C₈/SiO₂ interface, respectively. The L_{ii}^{surface} and $L_{ii}^{\text{interface}}$ ($i = y$ or z) are the Fresnel coefficients of the air/PTCDI-C₈ surface and the PTCDI-C₈/SiO₂ interface, respectively. It should be noted that they depend on the thickness of the film. The explicit forms of the Fresnel coefficients are given in Appendix A. Here, we suppose the relation between $\chi_{\text{yyz}}^{\text{surface}}$ and $\chi_{\text{yyz}}^{\text{interface}}$ is expressed as follows:

$$\chi_{\text{yyz}}^{\text{surface}} = c_2 e^{i\phi} \chi_{\text{yyz}}^{\text{interface}} \quad (4-8)$$

where c_2 and ϕ are a proportional constant and a relative phase between $\chi_{\text{yyz}}^{\text{surface}}$ and $\chi_{\text{yyz}}^{\text{interface}}$, respectively. Combining equation (4-3), (4-5) and (4-8), we have

$$\begin{aligned} A_q &\propto F_{\text{yyz}}^{\text{surface}} \chi_{\text{yyz}}^{\text{surface}} + F_{\text{yyz}}^{\text{interface}} \chi_{\text{yyz}}^{\text{interface}} \\ &= c_3 \left(c_2 e^{i\phi} F_{\text{yyz}}^{\text{surface}} + F_{\text{yyz}}^{\text{interface}} \right) \chi_{\text{yyz}}^{\text{interface}} . \end{aligned} \quad (4-9)$$

The quantity c_3 is also a proportional constant. The amplitude A_q depending on the PTCDI-C₈ film thickness can then be fitted using equation (4-10)

$$F = \left| c_3 \left(c_2 e^{i\phi} F_{\text{yyz}}^{\text{surface}} + F_{\text{yyz}}^{\text{interface}} \right) \right|. \quad (4-10)$$

So far the bulk contribution has been neglected due to the electric-dipole approximation, where an SFG process is forbidden in a centrosymmetric medium. But, if we take higher order terms into consideration, even for an isotropic or a centrosymmetric

bulk, there can be a nonnegligible contribution to SFG or SHG signals from the bulk term based on electric quadrupole and magnetic dipole form [3-5]. For the simplest case of an isotropic substance, the nonlinear bulk response can be treated as a scalar parameter [6]. The equation (4-9) can then be modified to the form

$$A_q \propto F_{yyz}^{\text{surface}} \chi_{yyz}^{\text{surface}} + F_{yyz}^{\text{interface}} \chi_{yyz}^{\text{interface}} + F_{yyz}^{\text{bulk}} \chi_{yyz}^{\text{bulk}} \quad (4-11)$$

with

$$F_{yyz}^{\text{bulk}} = \int_{-D}^0 \left[\exp\{-i(w_2^{\text{SF}} + w_2^{\text{Vis}} + w_2^{\text{IR}})z_0\} L_{yy}^{\text{bulk}}(\omega_{\text{SF}}, z_0) L_{yy}^{\text{bulk}}(\omega_{\text{Vis}}, z_0) L_{zz}^{\text{bulk}}(\omega_{\text{IR}}, z_0) \sin \beta_{\text{IR}} \right] dz_0 \quad (4-12)$$

where D is the thickness of the PTCDI-C₈ layer; z_0 is a z position inside the PTCDI-C₈ film; w_2^{SF} , w_2^{Vis} , w_2^{IR} are the z -component of wavevectors of the SFG signal, visible probe and IR probe in the z direction within the PTCDI-C₈ bulk, respectively. Equation (4-12) integrates the contribution from material at z_0 , taking into the phase mismatch effect. χ_{yyz}^{bulk} quantifies the bulk contribution per volume unit and is measured relative to $\chi_{yyz}^{\text{interface}}$ as follows

$$\chi_{yyz}^{\text{bulk}} = c_4 e^{i\psi} \chi_{yyz}^{\text{interface}} \quad (4-13)$$

where c_4 and ψ denote a proportional constant and a relative phase between χ_{yyz}^{bulk} and $\chi_{yyz}^{\text{interface}}$, respectively. As is the case with the fitting equation without the bulk contribution, the fitting equation for A_q depending on the film thickness can be written as

$$F = \left| c_3 \left(c_2 e^{i\phi} F_{yyz}^{\text{surface}} + F_{yyz}^{\text{interface}} + c_4 e^{i\psi} F_{yyz}^{\text{bulk}} \right) \right|. \quad (4-14)$$

Fitting thickness-dependent A_q with eq. (4-14) may allow us to determine separately the bulk and interface contributions to the resonant SFG amplitudes.

4.4 Results and Discussion

Figure 4.2 shows vibrational SFG spectra of PTCDI-C₈ thin layers with different thicknesses on SiO₂ substrates as well as fitting results on each spectrum measured with ssp polarization combination. The SFG intensities were normalized against that of a GaAs(110) substrate. The vibrational bands observed at 1695 and 1659 cm⁻¹ are assigned to the symmetric and antisymmetric stretching vibrations of carbonyl group in the imide groups, respectively [7]. The fitting analysis of a series of SFG spectra was conducted to extract the band amplitudes. The standard model function for SFG spectra (eq. (4-4)) was used. In the analysis, we assumed that the resonant wavenumber and bandwidth for each vibrational band were the same in all the SFG spectra. The thickness dependences of the band amplitudes are shown in Figure 4.3 (a) and (b). The 1695-cm⁻¹ band steadily increases in intensity between 0- and 50-nm thicknesses, while it stays constant between from 50 to 250 nm in thickness. On the other hand, the SFG intensity of the 1659-cm⁻¹ band gradually increases as the PTCDI-C₈ film grows in thickness.

In order to extract information about the source of the observed SFG signal of PTCDI-C₈ thin films from the observed thickness dependences, we conducted analyses based on the Fresnel coefficients. The basic assumption on the analyses is that the molecular structures at the air/PTCDI-C₈ interface, the PTCDI-C₈/SiO₂ interface, and in PTCDI-C₈ bulk are independent of the film thickness. To analyze the observed thickness dependence of the amplitudes of carbonyl stretches, the Fresnel coefficients of the bands were calculated. Shown in Figure 4.4 (a) and (c) are the calculated absolute values of Fresnel coefficients for the 1695-cm⁻¹ and 1659-cm⁻¹ bands of the air/PTCDI-C₈ surface and PTCDI-C₈/SiO₂ interface with eqs. (4-6) and (4-7) (see Appendix for more details). The parameters used in the calculation are summarized in Table 4.2. In the calculation, refractive indices for interfacial layers (n_{sur} or n_{int}) were assumed to be equal to that of bulk PTCDI-C₈ material. Fresnel coefficients considerably vary with the film thickness. The thickness dependences of the observed SFG band amplitudes (Figure 4.4 (a) and (b)) do not

at all look like those of the Fresnel coefficients for the two interfaces. The dissimilarity indicates that the source of SFG signal could not be restricted only to one interface and the detected SFG signals were interference results of the signals generated from both interfaces. That is, constructive or destructive signal interferences may occur.

To gain insight into the interference patterns, we used eq. (4-10) which gives the ratio of the SFG amplitude of the air/PTCDI-C₈ surface to that of the PTCDI-C₈/SiO₂ interface. Based on the assumption, the factors c_2 and c_3 in eq. (4-9) and (4-10) would not change as a function of the film thickness, while F_{yyz}^{surface} and $F_{yyz}^{\text{interface}}$ would vary when the film thickness is changed. The model function was fitted to the observed thickness dependences with the least squares method and the fitting parameters (c_2 , c_3 , and ϕ) were obtained. Figure 4.3 (a) and (b) also present the fitting results with eq. (4-10). The overall behaviors were reproduced by the fitting results. The fitting parameters were obtained as shown in Table 4.1 (the column without the bulk contribution). In Figure 4.3 (c) and (d), the contribution from the air/PTCDI-C₈ interface and that from the PTCDI-C₈/SiO₂ interface, $|c_2 e^{i\phi} F_{yyz}^{\text{surface}}|$ and $|F_{yyz}^{\text{interface}}|$, are shown with the most probable values of the fitting parameters to estimate the contributions from each interface to SFG amplitudes. As seen in Figure 4.3 (c), the relative contribution of the air/PTCDI-C₈ surface was slightly larger than that of the PTCDI-C₈/SiO₂ interface for the film thickness less than 50 nm for the 1695-cm⁻¹ band. For the film thickness greater than 50 nm, the relative contribution of the PTCDI-C₈/SiO₂ interface gradually decreases as the film thickness increases. The electronic absorption of the SFG signal and the visible probe beam by PTCDI-C₈ molecules should be the main reason for the rapid decrease of the contribution of the PTCDI-C₈/SiO₂ interface. The similar tendency can be seen for the 1659-cm⁻¹ band except for the point that the relative contribution of the air/PTCDI-C₈ surface is slightly larger than that for the 1695-cm⁻¹ band. The relative phase (ϕ) between the two interfaces were determined around π radian for both bands. The π radian phase

suggests that the atomic groups responsible for the signal were oppositely oriented at the two interfaces for the sign of the second order susceptibility for SFG is inverted when the orientation of the molecular system is inverted. In this way, it is shown that the observed thickness dependences of the SFG band amplitudes are understandable as the coherent sum of radiation fields from the two interfaces.

Thus far we have restricted our attention to SFG only from the interfaces. However, even a centrosymmetric medium can contribute to SFG signals via induced higher-order terms, including electric quadrupole and magnetic dipole. This means that the PTCDI-C₈ bulk can also contribute to the interference of SFG signals and accordingly modulate the thickness dependence of the SFG amplitudes. The analysis that includes the bulk contribution has been conducted based on eq. (4-14). Figure 4.4 (b) and (d) show the calculated modulus of the Fresnel coefficient of the PTCDI-C₈ bulk with eq. (4-12) for the two bands. Contrast to the contributions from interfaces, the bulk contribution is zero for zero thickness. Then, eq. (4-14) was adopted for the fitting function of the SFG amplitudes to estimate the contributions of the bulk besides the two interfaces. The SFG amplitudes and fitting results with eq. (4-14) are shown in the upper panel of Figure 4.5. The fitting parameters are listed in Table 4.1 (the column with the bulk contribution). The contributions from the two interfaces and the bulk ($c_2 e^{i\phi} F_{yyz}^{\text{surface}}$, $|F_{yyz}^{\text{interface}}|$, $c_4 e^{i\psi} F_{yyz}^{\text{bulk}}$) were plotted in Figure 4.5 (c) and (d). Compared with the fitting result without the bulk contributions for each band, the fitting results with the bulk contribution were not improved so much. Therefore, we can not conclude whether the bulk contributes to the SFG signal or not solely on the comparison of the fitting results with and without the bulk contribution. However, it should be noted that even in the fitting results with the bulk contribution, the contribution of the PTCDI-C₈ bulk is not so large that it overwhelms the contributions of the two interfaces. In other words, it can safely be said that the SFG signals from each of the interfaces contain substantial information on interfacial molecular structures.

An effective way to see whether the SFG signal does not be dominated by the bulk contribution is to perturb the surface and examine the spectral changes. Similar experimental approaches to various surfaces have been reported in the literatures [8-11]. The spectrum is not expected to change by the surface perturbation if the signal from the bulk overwhelms the whole observed SFG signal. To check this point, the isotropic polystyrene thin layer was formed on the PTCDI-C₈ sample by spin coating, and the SFG spectral change between before and after the film formation were examined. The 0.01 mM cyclohexane solution of polystyrene (Sigma-Aldrich, molecular weight: 200,000) was used to obtain the polystyrene film. It was dropped on the substrate to be spin-coated at 500 RPM for 60 seconds. The film thickness was roughly estimated to be about 80 nm with the aid of the electronic absorption spectrum of the polystyrene film on a CaF₂ substrate made by the same spin-coating method. Figure 4.6 shows the sps polarized SFG spectra of the sample measured before and after the treatment. The visible probe wavelength was 530 nm. On the spectra, besides the overall intensity change, the relative band intensities of the 1695-, 1590- and 1575-cm⁻¹ bands were greatly changed after the film formation. The observed relative band intensity change indicates that the polystyrene layer perturbed the molecular structure at the topmost part of the PTCDI-C₈ film, which corresponds to the air/PTCDI-C₈ surface before polystyrene over-coating, strongly suggesting that the SFG signal of the PTCDI-C₈ sample without the coating came partly from the air/PTCDI-C₈ surface without being overwhelmed by the contribution from the bulk.

4.5 Conclusion

In this chapter, we have applied SFG spectroscopy to the PTCDI-C₈ thin film deposited on a SiO₂ substrate. The SFG spectra were measured for the PTCDI-C₈ samples with different PTCDI-C₈ film thicknesses. The thickness-dependent SFG amplitudes of each vibrational band were analyzed assuming that molecular structures at the interfaces and bulk are independent of the film thickness. In the analysis, the model functions for the effective susceptibility of the sample were constructed based on the Fresnel coefficients. We examined the thickness dependence with two types of function. One of them includes only the interfacial contributions from the air/PTCDI-C₈ and PTCDI-C₈/SiO₂ interfaces, and the other also includes the bulk contribution of the PTCDI-C₈ layer. The former can be justified under the electric-dipole approximation, and the latter involves a higher order contribution beyond the approximation. Although the possible contribution from the bulk could not be excluded, it was concluded that the bulk contribution does not overwhelm those from the interfaces. This suggestion was supported by the results of the SFG spectral response to a surface perturbation by polystyrene film formation on the sample.

In this research, DR-SFG spectroscopy could be the promising approach to obtain the interfacial information. I hope that I will extend this work to the quantitative analysis of the molecular orientation of the PTCDI-C₈/SiO₂ interface by deconvoluting the information from the interfaces and bulk.

Appendix. Fresnel coefficients for organic thin films on substrates

In this appendix, the explicit formulas of the Fresnel coefficients will be given. The assumed model of the sample and the definition of a coordinate system are shown in Figure 4.7. Media 1, 2 and 3 represent the air, PTCDI-C₈, SiO₂, respectively. n_1 , n_2 and n_3 are refractive indices of air, PTCDI-C₈ and SiO₂, respectively. θ_1 is the incident angle in air. θ_2 and θ_3 denote the real angles of refraction in the PTCDI-C₈ film and SiO₂ layer, respectively. n_{sur} and n_{int} refer to the refractive indices in the air/PTCDI-C₈ surface and PTCDI-C₈/SiO₂ interface, respectively. The thickness of the PTCDI-C₈ film is D . It is assumed that the permeabilities of all the materials constituting each layer are 1.

The refractive index of a medium becomes complex when the media absorbs light. Snell's law holds even for media whose refractive indices are complex. However, in a case of complex refractive indices, a refractive angle may become complex. In general, the real part of a complex refractive angle ϕ is not the real angles of refraction θ , which is defined as the angle between the interface normal and the plane of constant phase [12]. Snell's law was adopted to calculate real numbers of θ_2 and θ_3 for the IR probe. On the other hand, for the 530-nm probe, Snell's law gives the complex refractive angle ϕ_2 , because refractive index of media 2 for the visible light is complex. For the 530-nm probe, for example, the real refractive angle is calculated as follows [12]. In this case, n_1 is real but n_2 is complex. The following three equations [12] hold:

$$k_1 \sin \theta_1 = k_2 \sin \theta_2, \quad (4-15)$$

$$k_2^2 - \alpha_2^2 = \left\{ (n')_2^2 - \kappa_2^2 \right\} k_1^2, \quad (4-16)$$

$$k_2 \alpha_2 \cos \theta_2 = (n')_2 \kappa_2 k_1^2, \quad (4-17)$$

where k_1 is the magnitude of wavevector in air; k_2 and α_2 are magnitudes of the real part and imaginary part of the wavevector amplitude in the PTCDI-C₈ film, respectively; $(n')_2$ and κ_2 are the real part and imaginary part of the refractive index in the PTCDI-C₈ film, i.e., $n_2 = (n')_2 + i\kappa_2$. By solving the three equations, k_2 , α_2 , and θ_2 can be obtained. ϕ_2 for the

visible probe can be obtained by eq. (4-18),

$$n_2 = \frac{k_2 \cos \theta_2 + i\alpha_2}{k_1 \cos \phi_2}. \quad (4-18)$$

Note that ϕ_2 can also be obtained using Snell's law ($n_1 \sin \theta_1 = n_2 \sin \phi_2$). ϕ_3 for the visible probe can be derived by eq. (4-19),

$$n_2 \sin \phi_2 = n_3 \sin \phi_3. \quad (4-19)$$

where n_3 and ϕ_3 are the complex refractive index and complex refractive angle in the SiO₂ layer, respectively.

To derive angles for an SFG signal in all the media, first the angle of the SFG in medium 2 ($\theta_{2,SF}$) should be calculated. Eqs. (4-16) and (4-17) hold for SFG signal. However, instead of eq. (4-15), the following phase matching condition in medium 2 is used:

$$k_{2,SF} \sin \theta_{2,SF} = k_{2,Vis} \sin \theta_{2,Vis} + k_{2,IR} \sin \theta_{2,IR}, \quad (4-20)$$

where $k_{2,SF}$ and $k_{2,Vis}$ are the magnitudes of the real parts of the complex wavevector amplitudes of the SFG signal and visible probe, respectively; $k_{2,IR}$ is the magnitude of the real wavevector amplitude of the IR probe; $\theta_{2,SF}$ is the output angle for the SFG signal in the PTCDI-C₈ film; $\theta_{2,Vis}$ and $\theta_{2,IR}$ are the real refractive angles for the visible probe and IR probe in the PTCDI-C₈ film, respectively. Solving eqs. (4-16), (4-17), and (4-20) simultaneously, $k_{2,SF}$, $\theta_{2,SF}$, and $\alpha_{2,SF}$, can be obtained. Then using eq. (4-18), the complex angle for SFG, $\phi_{2,SF}$, can be also calculated. The complex angles $\phi_{1,SF}$, $\phi_{3,SF}$, can be figured out using Snell's law:

$$n_1 \sin \phi_{1,SF} = n_2 \sin \phi_{2,SF} \quad (4-21)$$

$$n_2 \sin \phi_{2,SF} = n_3 \sin \phi_{3,SF} \quad (4-22)$$

With the method developed by Sipe and co-workers [6,13], the Fresnel coefficients for the PTCDI-C₈/SiO₂ interface (2/3 interface) were derived as follows:

$$L_{xx}^{\text{interface}} = \frac{t_{12}^p \exp(iw_2 D)(1 - r_{23}^p)}{1 + r_{12}^p r_{23}^p \exp(2iw_2 D)} \times \frac{\cos\phi_2}{\cos\phi_1}, \quad (4-23)$$

$$L_{yy}^{\text{interface}} = \frac{t_{12}^s \exp(iw_2 D)(1 + r_{23}^s)}{1 + r_{12}^s r_{23}^s \exp(2iw_2 D)}, \quad (4-24)$$

$$L_{zz}^{\text{interface}} = \frac{t_{12}^p \exp(iw_2 D)(1 + r_{23}^p)}{1 + r_{12}^p r_{23}^p \exp(2iw_2 D)} \times \frac{n_1 n_2}{n_{\text{int}}^2}, \quad (4-25)$$

where w_i corresponds to the z -component of the wavevector amplitude in i -th media and is given by

$$w_i = \frac{2\pi}{\lambda_0} n_i \cos\phi_i, \quad (4-26)$$

and t_{ij}^p , r_{ij}^p , t_{ij}^s , and r_{ij}^s are given by

$$t_{ij}^p = \frac{2w_i n_i n_j}{w_i n_j^2 + w_j n_i^2}, \quad (4-27)$$

$$r_{ij}^p = \frac{w_i n_j^2 - w_j n_i^2}{w_i n_j^2 + w_j n_i^2}, \quad (4-28)$$

$$t_{ij}^s = \frac{2w_i}{w_i + w_j}, \quad (4-29)$$

$$r_{ij}^s = \frac{w_i - w_j}{w_i + w_j}. \quad (4-30)$$

In Sipe's original equation, the refractive index of surface, n_{sur} , does not appear in L_{zz}^{surface} , but it can be converted into the form of eq. (4-24). The converted form can be used with Cartesian SFG tensors by the definition due to Heinz [14], which is widely used in the analysis of vibrational SFG spectra. Eqs. (4-23), (4-24) and (4-25) are identical with those reported in the literatures [15-17]. Fresnel coefficients for the air/PTCDI-C₈ surface (1/2 surface) can be derived in the same manner.

$$L_{xx}^{\text{surface}} = \frac{t_{12}^p \{1 - r_{23}^p \exp(2iw_2 D)\}}{1 + r_{12}^p r_{23}^p \exp(2iw_2 D)} \times \frac{\cos\phi_2}{\cos\phi_1} \quad (4-31)$$

$$L_{yy}^{\text{surface}} = \frac{t_{12}^s \{1 + r_{23}^s \exp(2iw_2 D)\}}{1 + r_{12}^s r_{23}^s \exp(2iw_2 D)} \quad (4-32)$$

$$L_{zz}^{\text{surface}} = \frac{t_{12}^p \{1 + r_{23}^p \exp(2iw_2 D)\}}{1 + r_{12}^p r_{23}^p \exp(2iw_2 D)} \times \frac{n_1 n_2}{n_{\text{sur}}^2} \quad (4-33)$$

These equations hold for both probe beams and an SFG signal in the reflection geometry with appropriate refractive indices. These three equations are also the same as the ones in the literatures [15-17]. The Sipe's approach can be applied to derive the Fresnel coefficients for the PTCDI-C₈ bulk. If a nonlinear polarization sheet lies in the $z = z_0$ plane, the Fresnel coefficients for probe beams and an SFG signal can be written as:

$$L_{xx}^{\text{bulk}}(z_0) = \frac{t_{12}^p \{ \exp(-iw_2 z_0) - \exp\{iw_2(2D + z_0)\} r_{23}^p \}}{1 + \exp(2iw_2 D) r_{12}^p r_{23}^p} \times \frac{\cos \phi_2}{\cos \phi_1}, \quad (4-34)$$

$$L_{yy}^{\text{bulk}}(z_0) = \frac{t_{12}^s \{ \exp(-iw_2 z_0) + \exp\{iw_2(2D + z_0)\} r_{23}^s \}}{1 + \exp(2iw_2 D) r_{12}^s r_{23}^s}, \quad (4-35)$$

$$L_{zz}^{\text{bulk}}(z_0) = \frac{t_{12}^p \{ \exp(-iw_2 z_0) + \exp\{iw_2(2D + z_0)\} r_{23}^p \}}{1 + \exp(2iw_2 D) r_{12}^p r_{23}^p} \times \frac{n_1}{n_2}. \quad (4-36)$$

We note that the three equations are identical with the ones reported by D. Wilk et al [18].

The refractive indices used to calculate the Fresnel coefficients are listed in Table 4.3. When Fresnel coefficients are calculated for the air/PTCDI-C₈ and PTCDI-C₈/SiO₂ interfaces, refractive indices at both interfaces are needed. Actually, the refractive indices of the interfacial layers may differ from that of the bulk [19,20]. However, we assumed that they are the same as that of the PTCDI-C₈ bulk in this study.

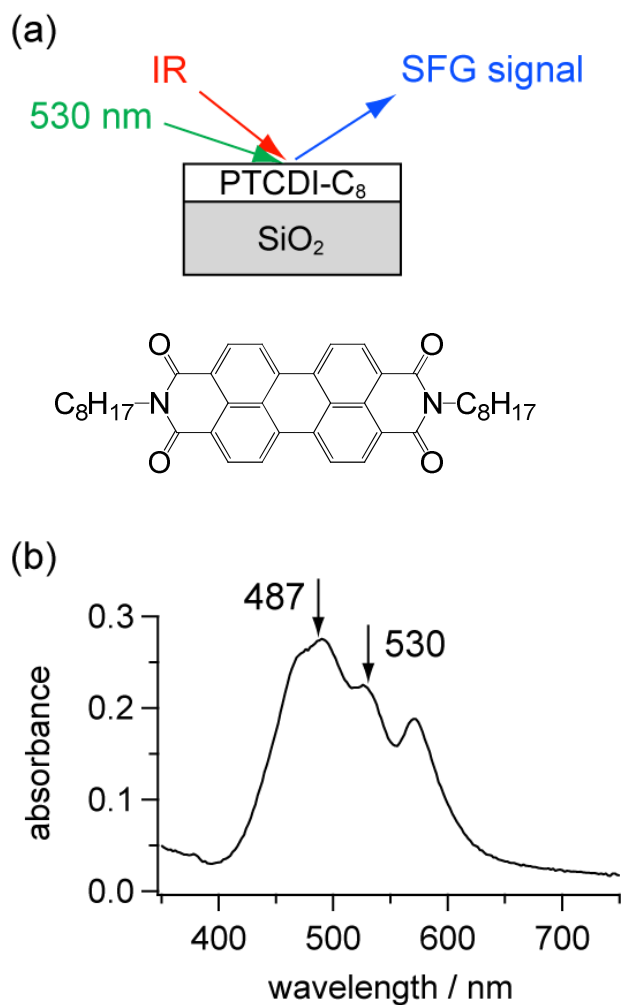


Figure 4.1 (a) schematic illustration of the SFG experimental geometry for the PTCDI-C₈ layer on a SiO₂ substrate and the structural formula of PTCDI-C₈. (b) electronic absorption spectrum of the PTCDI-C₈ layer of 50 nm thickness on a SiO₂ substrate. The numbers of 530 and 487 with arrows stand for the wavelength of the visible input beam and SFG signal (corresponding to the IR light of 1659 cm⁻¹), respectively.

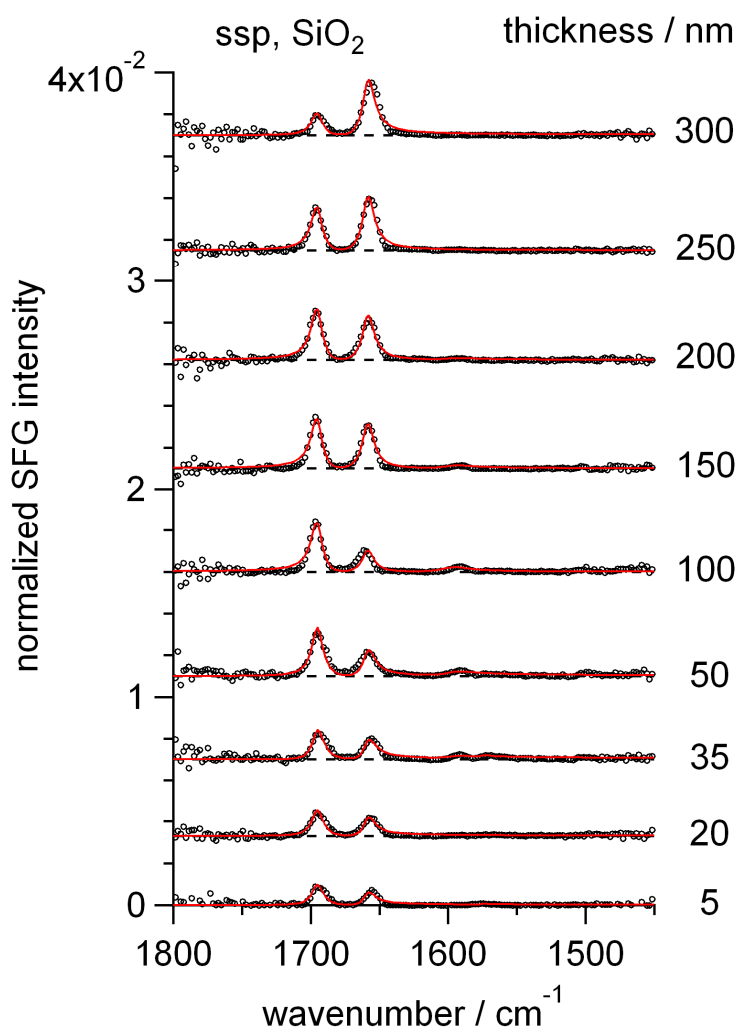


Figure 4.2 The ssp SFG spectra of the PTCDI-C₈ layers with different thicknesses on SiO₂ substrates. All the spectra were normalized against the signal from a GaAs(110) substrate. Circles are observed data and solid lines are fitting results to eq. (4-4). The dashed horizontal lines indicate the baselines for each spectrum.

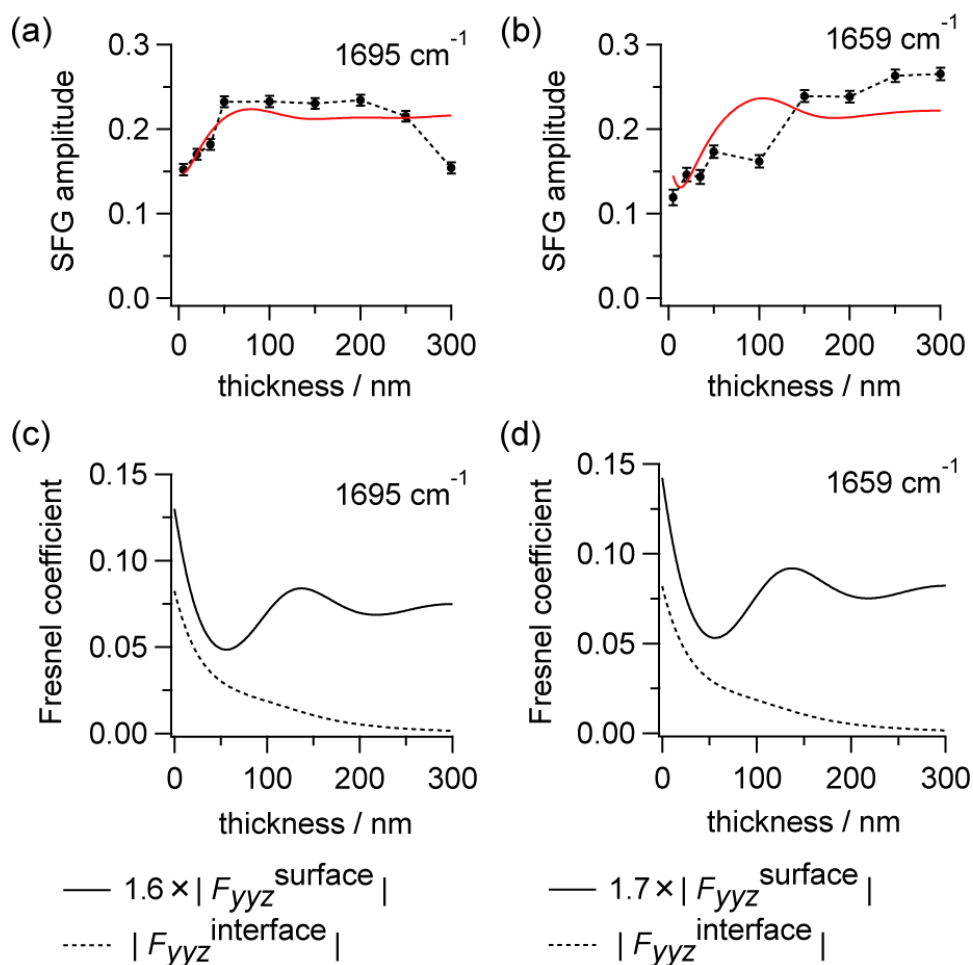


Figure 4.3 upper panel : SFG amplitudes (dotted line and circle) and fitting results (solid line) to eq. (4-10) for the PTCDI-C₈ films on SiO₂ substrates. (a) 1695 cm⁻¹ band (b) 1659 cm⁻¹ band
 lower panel : absolute Fresnel coefficients determined by the fitting with eq. (4-10). The dotted and solid lines stand for the contribution of the PTCDI-C₈/SiO₂ interface and the air/PTCDI-C₈ surface to the SFG amplitude, respectively. (c) 1695 cm⁻¹ band (d) 1659 cm⁻¹ band

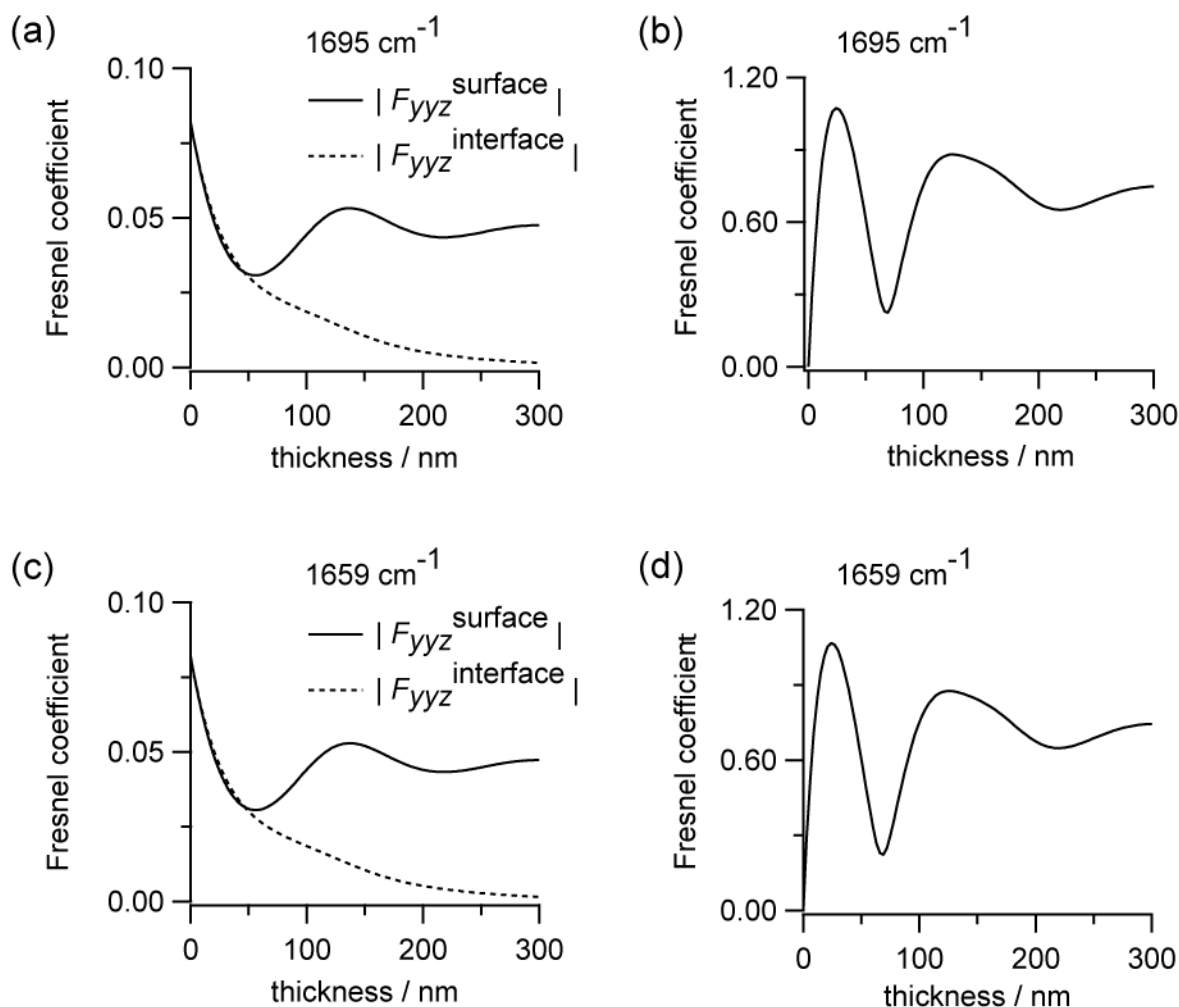


Figure 4.4 absolute Fresnel coefficients corresponding to the 1695 and 1659 cm⁻¹ bands calculated as a function of the PTCDI-C₈ thickness.

- (I) 1695 cm⁻¹ band; (a) the air/PTCDI-C₈ surface (solid line) and the PTCDI-C₈/SiO₂ interface (dotted line). (b) the PTCDI-C₈ bulk
- (II) 1659 cm⁻¹ band; (c) the air/PTCDI-C₈ surface (solid line) and the PTCDI-C₈/SiO₂ interface (dotted line). (d) the PTCDI-C₈ bulk

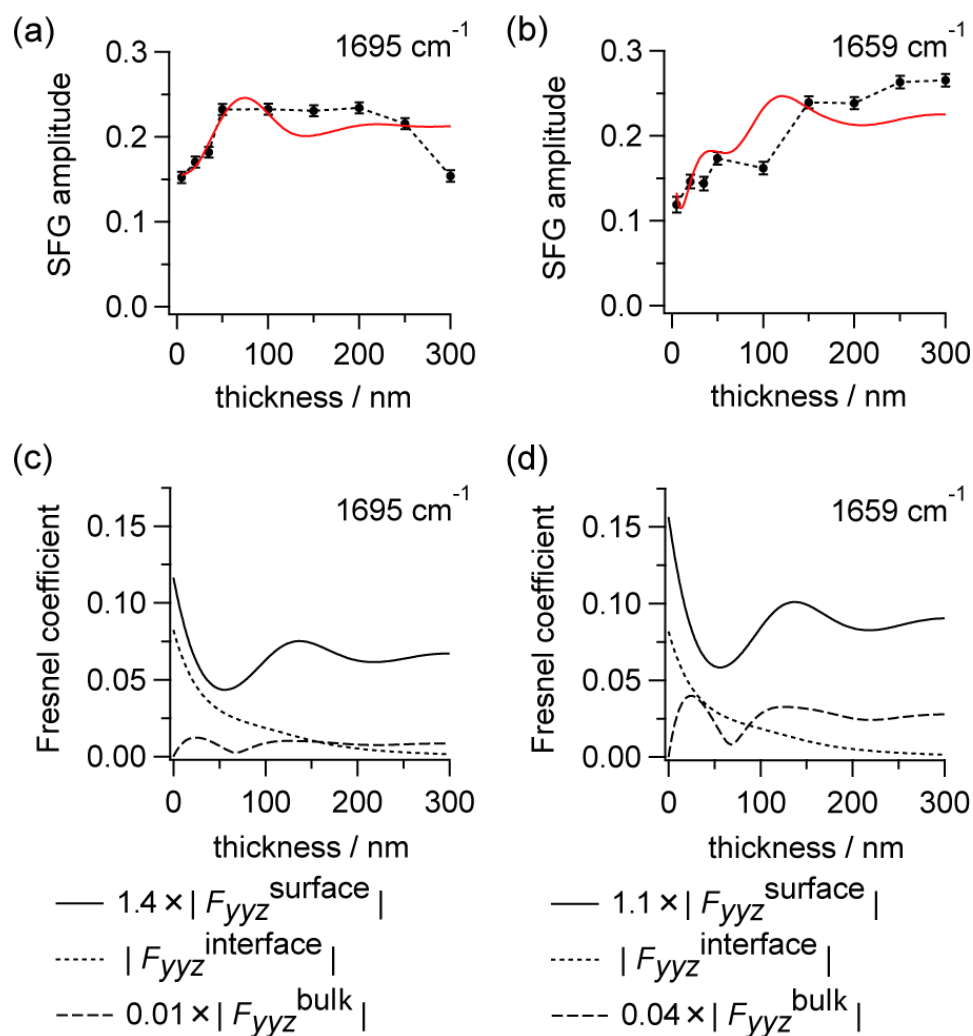


Figure 4.5 upper panel : SFG amplitudes (dotted line and circle) and fitting results (solid line) to eq. (4-14) for the PTCDI-C₈ films on SiO₂ substrates with the bulk contribution of the PTCDI-C₈ layer. (a) 1695 cm⁻¹ band (b) 1658 cm⁻¹ band

lower panel : absolute Fresnel coefficients determined by the fitting with eq. (4-14). The dotted line, solid line and dash line stand for the contributions of the PTCDI-C₈/SiO₂ interface, air/PTCDI-C₈ surface and PTCDI-C₈ bulk to the SFG amplitude, respectively. (c) 1695 cm⁻¹ band (d) 1659 cm⁻¹ band

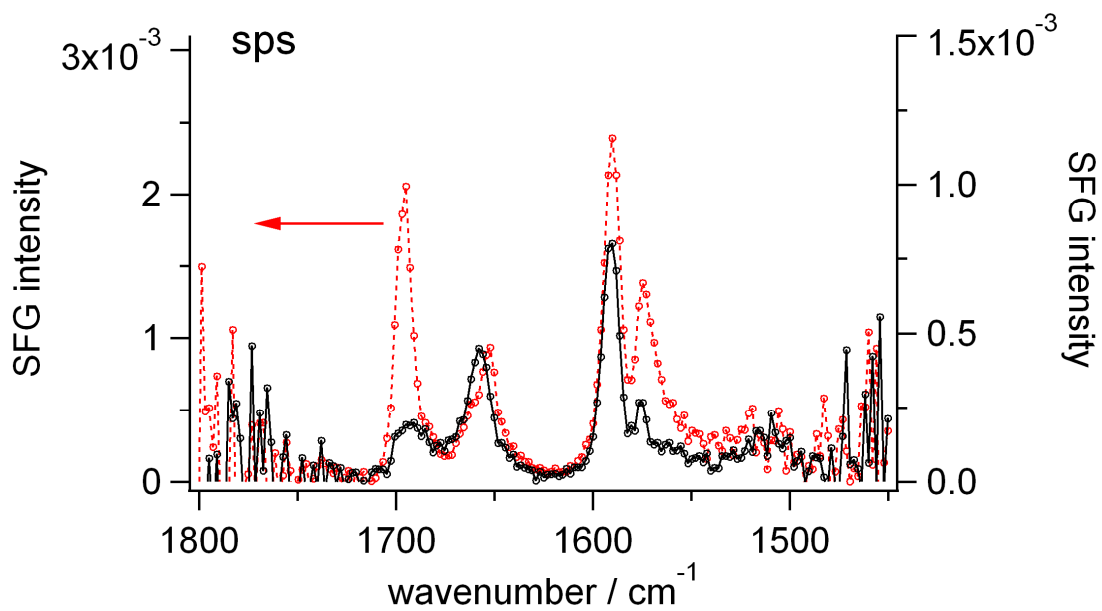


Figure 4.6 SFG spectra of the PTCDI-C₈ layer deposited on a SiO₂ substrate before (dashed line and circle) and after (solid line and circle) the spin-coating with sps polarization combination. The film thickness of the PTCDI-C₈ layer is 50 nm.

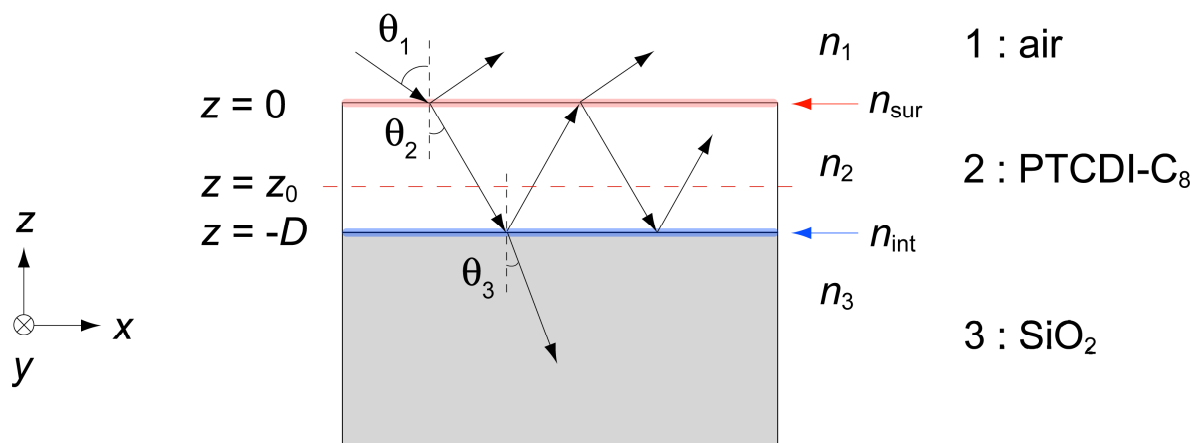


Figure 4.7 Schematic diagram of the PTCDI-C₈ layer deposited on a SiO₂ substrate.

| parameter | 1695-cm ⁻¹ band (CO sym. str.) | | 1659-cm ⁻¹ band (CO antisym. str.) | |
|----------------|---|------------------------|---|------------------------|
| | without bulk contribution | with bulk contribution | without bulk contribution | with bulk contribution |
| C ₂ | 1.6 ± 0.3 | 1.4 ± 0.6 | 1.7 ± 0.4 | 1.9 ± 1.0 |
| C ₃ | 2.9 ± 0.5 | 3.6 ± 1.5 | 2.8 ± 0.6 | 2.0 ± 1.8 |
| φ | 1.0π ± 0.1π | 0.9π ± 0.1π | 1.0π ± 0.1π | 1.2π ± 0.5π |
| C ₄ | | 0.01 ± 0.02 | | 0.04 ± 0.1 |
| ψ | | 1.3π ± 0.6π | | 0.5π ± 0.4π |

Table 4.1 Fitting parameters for the thickness-dependent SFG amplitudes of PTCDI-C₈ films on SiO₂ substrates.

| medium | refractive index | | | |
|---|--------------------------------|--------------------------------|-------------------------------------|-------------------------------------|
| | 487 nm | 530 nm | 5893 nm (1697 cm ⁻¹) | 6039 nm (1656 cm ⁻¹) |
| air | 1 | 1 | 1 | 1 |
| air/PTCDI-C ₈ surface | 1.717 + 0.507i (assumption) | 1.890 + 0.368i (assumption) | 1.486 (assumption) | 1.486 (assumption) |
| PTCDI-C ₈ | 1.717 + 0.507i ^[21] | 1.890 + 0.368i ^[21] | 1.486 ^[22] | 1.486 ^[22] |
| PTCDI-C ₈ /SiO ₂ interface | 1.717 + 0.507i (assumption) | 1.890 + 0.368i (assumption) | 1.486 (assumption) | 1.486 (assumption) |
| SiO ₂ | 1.463 ^[23] | 1.460 ^[23] | 1.278 ^[23] | 1.239 ^[23] |

Table 4.2 Refractive indices used in the calculation of Fresnel coefficients.

References

- [1] X. Zhuang, P. B. Miranda, D. Kim, Y. R. Shen, *Phys. Rev. B* **59**, 12632-12640 (1999).
- [2] Y. R. Shen, *Proc. Natl. Acad. Sci. U. S. A.* **93**, 12104-12111 (1996).
- [3] P. S. Pershan, *Phys. Rev.* **130**, 919-929 (1963).
- [4] E. Adler, *Phys. Rev.* **134**, A728-A733 (1964).
- [5] N. Bloembergen, R.K. Chang, S.S. Jha, C.H. Lee, *Phys. Rev.* **174**, 813-822 (1968).
- [6] V. Mizrahi, J. E. Sipe, *J. Opt. Soc. Am. B* **5**, 660-667 (1988).
- [7] Y. Hosoi, Y. Furukawa, *Mol. Cryst. Liq. Cryst.* **471**, 189-194 (2007).
- [8] Q. Du, R. Superfine, E. Freysz, Y. R. Shen, *Phys. Rev. Lett.* **70**, 2313-2316 (1993).
- [9] M. Oh-e, A. I. Lvovsky, X. Wei, Y. R. Shen, *J. Chem. Phys.* **113**, 8827-8832 (2000).
- [10] D. Kim, M. Oh-e, Y. R. Shen, *Macromolecules*, **34**, 9125-9129 (2001).
- [11] J. Wang, C. Chen, S. M. Buck, Z. Chen, *J. Phys. Chem. B* **105**, 12118-12125 (2001).
- [12] G. R. Fowles Ed., *Introduction to Modern Optics* (Dover Publications, New York, 1975)
- [13] J. E. Sipe, *J. Opt. Soc. Am. B* **4**, 481-489 (1987).
- [14] T. F. Heinz: *Nonlinear Surface Electromagnetic Phenomena*, Chap. 5, eds. H.-E. Ponath and G. I. Stegeman (Elsevier 1991)
- [15] X. Lu, N. Shephard, J. Han, G. Xue, Z. Chen, *Macromolecules* **41**, 8770-8777 (2008).
- [16] X. Lu, D. Li, C. B. Kristalyn, J. Han, N. Shephard, S. Rhodes, G. Xue, Z. Chen, *Macromolecules* **42**, 9052-9057 (2009).
- [17] C. B. Kristalyn, X. Lu, C. J. Weinman, C. K. Ober, E. J. Kramer, Z. Chen, *Langmuir*, **26**, 11337-11343 (2010).
- [18] D. Wilk, D. Johannsmann, C. Stanners, Y. R. Shen, *Phys. Rev. B* **51**, 10057-10067 (1995).
- [19] P. Ye, Y. R. Shen, *Phys. Rev. B* **28**, 4288-4294 (1983).
- [20] G. J. Simpson, C. A. Dailey, R. M. Plocinik, A. J. Moad, M. A. Polizzi and R. M. Everly, *Anal. Chem.* **77**, 215-224 (2005).

[21] Measured by a spectroscopic ellipsometry.

[22] Deduced by Cauchy dispersion formula.

[23] E. D. Palik Ed., *Handbook of Optical Constants of Solids*, Second Edition (Academic Press, New York, 1985).

Chapter 5. General Conclusion

In my thesis, a vibrationally-electronically doubly resonant SFG spectrometer has been developed to perform DR-SFG spectroscopy with a wide tunability of the visible and ultraviolet probes. By developing the spectrometer, the target molecules of the DR-SFG spectroscopy have been expanded into many aromatic molecules which have electronic absorption in the UV region. The dye molecules which have electronic absorption in the visible region are also the objects to be measured by DR-SFG spectroscopy. The spectrometer has been applied to the DR-SFG study of the monolayers on metal substrates, including a *p*-mercaptobenzoic acid (*p*-COOHC₆H₄SH) monolayer on gold (Chapter 2) and a fluorescein isothiocyanate isomer-I (FITC) monolayer on platinum (Chapter 3). The author also utilized DR-SFG spectroscopy to the research of the thin film consisting of N, N'-bis(octyl)perylene-3,4,9,10-tetracarboxylic diimide (PTCDI-C₈) deposited on a SiO₂ substrate (Chapter 4).

As shown in Chapter 2, the developed spectrometer has two main features. Firstly, the multiplex method was employed where broad-bandwidth (BB) IR and narrow-bandwidth visible probes were used to generate a BB SFG signal. Secondly, the probe wavelength for the visible probe can be chosen in a wide range of 235-390, 400, and 405-795 nm. To reduce stray light due to the scattering of the UV or visible probes, the prism monochromator instead of optical filters was adopted. The spectrometer permitted us to carry out DR-SFG spectroscopy in the UV region as well as in the visible region.

To check the performance of DR-SFG spectroscopy in the UV region, a *p*-COOHC₆H₄SH monolayer on a gold substrate was measured with 289- and 334-nm probes (Chapter 2). The electronic resonance effect enhanced the SFG intensity for both the carbonyl stretch mode and the phenyl ring stretch mode. I believe that the IR-UV DR-SFG spectroscopy will impact on the studies of aromatic molecules at various interfaces and broaden the scope of DR-SFG technique.

One of the main advantages of DR-SFG is the ability to identify chemical species at interfaces where various chemical species exist together by use of the electronic response

of the vibrational SFG signal. In Chapter 3, DR-SFG spectroscopy was conducted for a FITC monolayer on a platinum substrate to demonstrate the advantage mentioned above. Particular chemical species could be identified by comparing the DR-SFG excitation spectra of vibrational bands with electronic absorption spectra of the chemical species which is used to form the monolayer. As a result of the comparison, it was found that two chemical species (neutral and monoanion species) coexist on the platinum substrate. This estimation was supported by the interpretation of the spectral change of the monolayer with the alkaline treatment. The study proved that DR-SFG can be applied to identify chemical species at interfaces where various chemical species coexist.

The organic semiconductor (PTCDI-C₈) thin film deposited on a SiO₂ substrate was investigated by DR-SFG spectroscopy. The vibrational SFG spectra from the film whose bulk is centrosymmetric were obtained with a good signal-to-noise ratio. In Chapter 4, the source of the SFG signal was investigated. In order to examine the source of an SFG signal, the author measured SFG spectra of the PTCDI-C₈ films with different film thicknesses on SiO₂ substrates. The observed thickness-dependent SFG intensity was analyzed using model functions based on the Fresnel coefficients, assuming the molecular structures at interfaces and bulk are independent of the thickness. As a result, it is concluded that the observed signal substantially originated from the two interfaces (the air/PTCDI-C₈ and PTCDI-C₈/SiO₂ interfaces), suggesting DR-SFG have the potential to develop into a useful interface probe of organic thin films.

The availability and some advantages of DR-SFG spectroscopy have been demonstrated through all the study in my thesis. DR-SFG spectroscopy is a powerful technique to obtain much more interfacial information than singly resonant SFG spectroscopy. I hope that my works facilitate the progress of the DR-SFG spectroscopy and contribute to the development of the DR-SFG research field.

公表論文

(1) IR-UV Sum-Frequency Generation Spectrometer with a wide tunability of the UV probe

Toshiki Maeda and Taka-aki Ishibashi

Applied Spectroscopy, **61**, 459-464 (2007).

(2) Identification of chemical species of fluorescein isothiocyanate isomer-I (FITC) monolayers on platinum by doubly resonant sum-frequency generation spectroscopy

Toshiki Maeda, Tetsuhiko Nagahara, Misako Aida and Taka-aki Ishibashi

Journal of Raman Spectroscopy, **39**, 1694-1702 (2008).